Geometrically nonlinear refined shell theories by Carrera Unified Formulation

Geometrically nonlinear refined shell theories by Carrera Unified Formulation

B. Wu[a,b,*], A. Pagani[a,†], W.Q. Chen[c,‡], E. Carrera[a,d,§]

[a]Mul^2 Group, Department of Mechanical and Aerospace Engineering, Politecnico di Torino, 10129 Torino, Italy;

[b]School of Mathematics, Statistics and Applied Mathematics, NUI Galway, University Road, Galway, Ireland;

[c]Department of Engineering Mechanics, Zhejiang University, 310027 Hangzhou, China;

[d]Laboratory of Intelligent Materials and Structures, Tambov State Technical University, 392000 Tambov, Russia.

Abstract: In this work, a unified formulation of full geometrically nonlinear refined shell theory is developed for the accurate analysis of highly flexible shell structures. The tensor calculus is utilized to explicitly derive the linear and nonlinear differential operator matrices of the geometrical relation in the orthogonal parallel curvilinear coordinate system. By employing the Carrera Unified Formulation (CUF), various kinematics of two-dimensional shell structures are consistently formulated via an appropriate index notation and a generalized expansion of the primary variables by arbitrary functions in the thickness direction, leading to lower- to higher-order shell models with only pure displacement variables. Furthermore, the principle of virtual work and a finite element approximation are exploited to straightforwardly formulate the nonlinear governing equations in a *total Lagrangian* approach. Particularly, the path-following Newton-Raphson linearization method based on the arc-length constraint is used to deal with the full geometrically nonlinear problem. Independent of the theory approximation order, the forms of the fundamental nuclei of the secant and tangent stiffness matrices of the unified shell element are formulated via the CUF and the three-dimensional Green-Lagrange strain components. Numerical assessments and comparisons of the present results with those provided in the literature for popular benchmark problems involving different metallic shell structures are found to be excellent and demonstrate the capabilities of the developed CUF shell model to predict the post-buckling, large-deflection, snap-through and snap-back nonlinear responses with high accuracy.

Keywords: Carrera Unified Formulation; Refined shell theory; Geometrical nonlinearity; Large-deflection; Post-buckling; Snapping; Arc-length method.

---

1 Introduction

Owing to their superior advantages such as high strength-to-weight and stiffness-to-weight ratios, thin-walled structures with curvatures, better known as shells, are among the most significant and ubiquitous structural components vastly employed in modern engineering applications such as bridges, roofs, aircraft and spacecraft skins, rockets, and pressure vessels. Thus, a series of traditional theories have been established in the *linear* scenario to conduct the structural analysis of shells, including the classical shell

*Postdoctoral Fellow. E-mail: bin_wu@polito.it

†Assistant professor. E-mail: alfonso.pagani@polito.it

‡Professor of Engineering Mechanics. E-mail: chenwq@zju.edu.cn

§Professor of Aerospace Structures and Aeroelasticity. E-mail: erasmo.carrera@polito.it

theory [1] based on the Kirchhoff-Love assumptions, the first-order shear deformation theories (FSDT) [2] built on the Mindlin-Reissner assumption, and a variety of higher-order shear deformation theories (HSDT) [3, 4, 5]. Kapania and Raciti [6] and Carrera [7] comprehensively reviewed the modeling and analysis of laminated composite structures including shells. Currently, highly flexible shell structures are widely used in different structural components such as space antennas, solar sails, wing structures, and rotor blades in aeronautical engineering [8], flexible robotic arms in mechanical engineering, submarine hulls in naval industry, soft tissues and advanced instrument in biological engineering [9], flexibel phononic crystals and metamaterials in reconfigurable and wave devices [10, 11, 12], to name a few. On one hand, these highly flexible structures are prone to suffering large-deflection, post-buckling and snapping behaviors when subjected to severe environmental conditions and large loadings. On the other hand, some aircraft structural components (such as fuselage, wing, and stabilizer panels) and flexible mechanical metamaterials are able to operate properly beyond the buckling range and have a post-buckling strength [10, 13, 14]. As a consequence, accurate predictions of the in-service nonlinear response of highly flexible structures in the geometrically nonlinear regime are of prime importance for their failure evaluation and rational employment.

Nowadays, considerable works have been focusing on the problem of how to develop excellent *two-dimensional (2-D) theories* in the *geometrically nonlinear* scenario for modeling the flexible structures. Among the 2-D theories, the simplest theory is the classical Kirchhoff-Love type theory [14, 15, 16, 17] that neglects the transverse shear deformation and cannot yield accurate results for the nonlinear analysis of elastic plates/shells. In fact, the shear deformations become more significant for the increasing thickness-to-width ratio and anisotropy as well as for the presence of geometrical nonlinearities. In order to improve the accuracy of the classical theory, much effort has been made to seek for the 2-D modified and refined structural theories to investigate the effect of the transverse shear strains on the geometrically nonlinear response of (moderately) thick and anisotropic plate/shell structures. In particular, contributions to the development of FSDT combined with different thickness stretching effects and various geometrically nonlinear theories (such as the von Kármán assumption) have been made to study the large-deflection, post-buckling and snapping behaviors of different shapes of metallic and composite structures under various combinations of edge support conditions and loadings [18, 19, 20, 21, 22, 23, 24, 25, 26]. Nonetheless, a uniform shear distribution across the thickness direction is assumed in the FSDT and thus the shear correction factors have to be introduced to adjust the transverse shear stiffness. Consequently, to avoid the shear correction factors appearing in the FSDT and accurately predict the distribution of the transverse shear strains/stresses in the thickness direction, several 2-D HSDT and refined theories along with different nonlinear strain assumptions have been proposed for the enhancement of transverse shear stress distributions in the geometrically nonlinear analysis of flexible thin-walled structures [13, 27, 28, 29, 30, 31, 32].

In addition to the modification and improvement of the transverse shear deformation, special attention has been devoted to higher-order theories of plates/shells accounting for the *thickness stretching effect* in the geometrically nonlinear analysis, which is a necessity when the significant thickness deformation is present in flexible or soft structures subjected to large deflections [10, 26]. The classical 5-parameter shell formulation [33] with Reissner-Mindlin kinematical assumptions, based on the degenerated shell concept and consistent with the FSDT of 2-D shell model [34], postulates a plane stress state and enforces the inextensibility condition of transverse normals by introducing a rotation tensor to analyze finite rotations [24]. As a result, it is not suitable to describe the large-displacement problems with the considerable thickness change of shell structures. In order to allow the thickness stretch of shells and maintain the fully three-dimensional (3-D) constitutive law, the 6-parameter shell model can be developed by adding an additional degree of freedom, but its implementation is unfortunately accompanied by the thickness locking or Poisson locking phenomenon (i.e. constant normal strain through the thickness) [23, 35], which is due to the artifact of the 6-parameter shell-theory formulation rather than the discrete finite element formulation in contrast to the classical 'shear locking' effect. Therefore, the so-called 7-parameter model accounting for the thickness stretching and mitigating the Poisson locking due to the quadratic expansion of the transverse displacement has been proposed with unmodified fully 3-D constitutive equations in the FSDT sense [22, 23, 24, 36]. In recent years, a large number

of higher-order thickness stretching models have been developed within the framework of the HSDT of plates/shells to provide a better prediction and evaluation of the thickness deformation of the flexible structures in the geometrically nonlinear regime [31, 32, 37, 38].

Furthermore, contributions have been made to developing different *geometrically nonlinear theories* (such as finite, moderate and small rotations, the von Kármán approximations, etc.) [23, 34, 39, 40, 41] into the higher-order shear deformation or/and thickness stretching models to effectively explore the geometrically nonlinear responses of plates/shells, which is challenging but plays a crucial role in the design, manufacturing, and application of flexible structures. Nevertheless, it should be emphasized that various approximations of geometrically nonlinear relations can result in different application ranges with certain limitation conditions. For example, the von Kármán type geometrically nonlinear theory inherently hypothesizes that only those nonlinear terms related to the in-plane partial derivatives of the transverse displacement are reserved in the strain-displacement relation, which could provide physically acceptable predictions for *thin* plates/shells with *moderate* rotations. However, the accuracy of von Kármán approximations could be not ensured for the *thick* structures with *large* rotations, especially in the case of shear loadings [41, 42]. On the contrary, based on the assumption of layerwise linear displacement distribution through thickness, the full geometrically nonlinear kinematic relations was considered by Kim and Chaudhuri [40] in a total Lagrangian approach to demonstrate the stable nonlinear equilibrium curves of laminated cylindrical panels, and it was pointed out that the von Kármán nonlinear strain approximation overestimates the transverse displacements for the same loadings, especially in the advanced nonlinear range. Thus, some investigations contain all nonlinear terms of the Green-Lagrange strain tensor in the framework of the higher-order and refined models to conduct the full geometrically nonlinear analysis [26, 42, 43, 44, 45, 46, 47].

To the authors' best knowledge, no general theoretical framework is available from the open literature to take account of the higher-order shear deformation, thickness stretching effects and even refined models into the full geometrically nonlinear analysis of *shell* structures in a unified way. This provides the motivation for the present work. It is worth mentioning that, based on the Carrera Unified Formulation (CUF) and the total Lagrangian description, the refined and full geometrically nonlinear beam and plate theories have been established to analyze the large displacement/rotation and post-buckling responses for both metallic and composite beam/plate structures [42, 45, 46] and to assess the effectiveness of different geometrically nonlinear strain approximations in the beam case [47]. When combined with a numerical incremental method, the *total Lagrangian* description has some superiorities compared with the *Eulerian* and *updated Lagrangian* approaches [43, 47, 48, 49]: (1) The numerical error will not be accumulated since the accuracy at the current solution step is independent of the solution at the previous step; (2) There is no necessity to conduct the coordinate transformation of stress and strain components during iteration; (3) With no loss of accuracy, it allows large loading steps and reverse analysis for the convergent solutions.

After an assessment of available works in the literature for the analysis of shells, the primary objective of the present study is to generalize the CUF beam/plate models [42, 45] for developing a full geometrically nonlinear refined and unified *shell* theory in the *total Lagrangian* approach to accurately predict the geometrically nonlinear responses (including large-deflection, post-buckling and snapping behaviors) of flexible shell structures. The proposed CUF shell model employs only pure displacement variables as the independent ones, which is convenient in terms of calculus stability and mesh manipulation. Owing to the intrinsic scalable nature of CUF [5, 50], the nonlinear governing equations and the related finite element (FE) arrays can be conveniently and straightforwardly constructed to obtain the refined and full geometrically nonlinear structural theory through the fundamental nuclei (FNs), a core unit of the structural stiffness matrix whose form is independent of the kinematics assumptions. The adopted kinematic theories can be treated as the input parameters to the FE analysis, resulting in a variety of lower- and higher-order FE models.

This paper is organized as follows. Sec. 2 employs the tensor analysis of curved surfaces to explicitly derive the linear and nonlinear differential operator matrices of the geometrical relation in the orthogonal parallel curvilinear coordinate system, and presents a brief description of the unified finite shell elements based on CUF. By utilizing the principle of virtual work in the total Lagrangian description, Sec. 3

derives the nonlinear equilibrium equations and the FNs of the *secant* stiffness matrix of the proposed unified geometrically nonlinear shell model. The path-following incremental linearized method with the arc-length constraint is briefly reviewed in Sec. 4, where the FNs of the *tangent* stiffness matrix are also obtained. Numerical examples are finally provided in Sec. 5 to evaluate the performance of the proposed unified shell elements in solving some challenging benchmark problems with geometrical nonlinearities taken from the literature, while some concluding remarks are made in Sec. 6.

2 Unified finite shell elements with geometrical nonlinearity

2.1 Geometrical description of the shell reference configuration

Consider a deformable continuum $\mathcal{B}$ that occupies in the Euclidean space a region $\mathcal{B}_r$ in the undeformed "reference configuration" at initial time t_0. At time t, the body $\mathcal{B}$ will occupy a region $\mathcal{B}_t$ in the "current configuration", if subjected to certain mechanical loading. A shell structure is by definition a deformable body with one geometric dimension of both regions $\mathcal{B}_r$ and $\mathcal{B}_t$ being significantly smaller than the other two. Its smaller dimension is called thickness. In this work, since the total Lagrangian description is adopted to formulate the unified finite shell elements with geometrical nonlinearity, we will briefly review the geometrical description of the shell reference configuration $\mathcal{B}_r$. For more details about the mathematical definitions and geometrical formulations of shells, the interested readers are referred to the chapter of Naghdi [2] and the monograph of Green and Zerna [51].

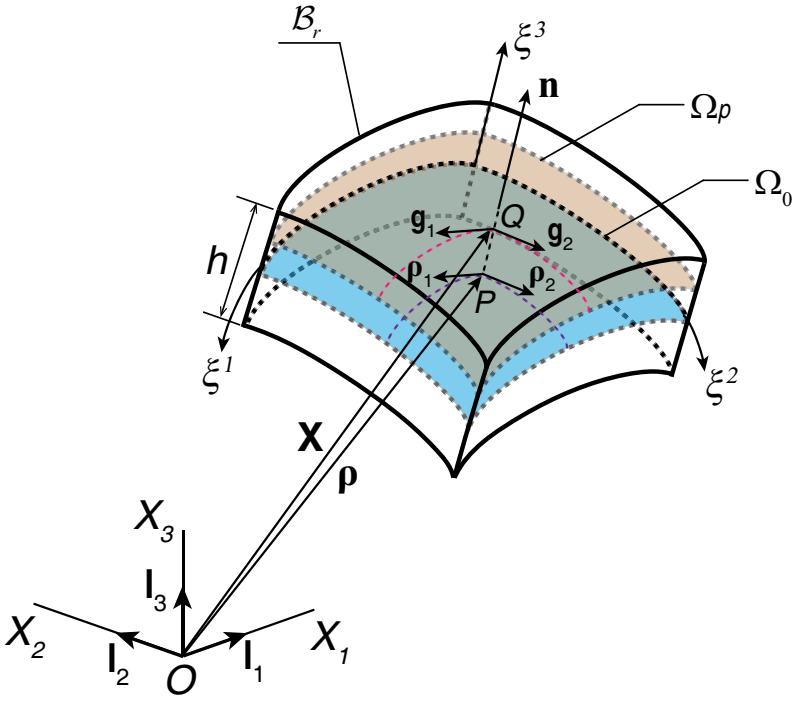

Figure 1: Geometrical description of an arbitrarily curved shell in the undeformed reference configuration with the parallel curvilinear coordinate system (ξ^1, ξ^2, ξ^3). The covariant basis vectors $\mathbf{g}_\alpha$ and $\boldsymbol{\rho}_\alpha$ on the parallel surface Ω_p and the mid-surface Ω_0 as well as the unit normal vector $\mathbf{n}$ are shown.

As shown in Fig. 1, an arbitrarily curved shell can be considered as a solid medium geometrically defined by a mid-surface Ω_0 (where Ω_0 is the reference or undeformed mid-surface of the shell) immersed in three-dimensional (3D) physical space and a *constant* thickness parameter h of the medium around the mid-surface. A parallel curvilinear coordinate system (ξ^1, ξ^2, ξ^3) is constructed within the shell structure, where ξ^1 and ξ^2 are two parametric curves which define the parallel surfaces, and the coordinate ξ^3 is chosen to be along the *common* unit normal vector $\mathbf{n}$ to the surfaces with $\xi^3 \in [-h/2, h/2]$. The surface $\xi^3 = 0$ defines the mid-surface Ω_0 of the region $\mathcal{B}_r$ while $\xi^3 \neq 0$ defines one parallel surface Ω_p. We take two arbitrary material points P and Q on the mid-surface Ω_0 and the parallel surface Ω_p, respectively.

Point Q lies directly above P in the direction of the unit normal vector $\mathbf{n}$. The position vectors $\boldsymbol{\rho}$ (point P) and $\mathbf{X}$ (point Q) given with respect to a fixed orthonormal Cartesian coordinate system with unit basis vectors $\mathbf{I}_i (i = 1, 2, 3)$ can be connected via parametrization as

$$\mathbf{X}\left(\xi^1, \xi^2, \xi^3\right) = \boldsymbol{\rho}\left(\xi^1, \xi^2\right) + \xi^3 \mathbf{n}\left(\xi^1, \xi^2\right). \tag{1}$$

For each point of the *shell volume* $\mathcal{B}_r$, we can use the position vector $\mathbf{X}$ to define the 3-D natural (or covariant) base vectors $\mathbf{g}_i$, dual (or contravariant) base vectors $\mathbf{g}^i$ and components g_{ij}, δ_i^j , g^{ij} of the metric tensor as

$$\begin{aligned} &\mathbf{g}_i = \frac{\partial \mathbf{X}}{\partial \xi^i} = \mathbf{X}_{,i}, \quad (i = 1, 2, 3), \\ &\mathbf{g}_i \cdot \mathbf{g}^j = \delta_i^j, \quad g_{ij} = \mathbf{g}_i \cdot \mathbf{g}_j, \quad g^{ij} = \mathbf{g}^i \cdot \mathbf{g}^j, \end{aligned} \tag{2}$$

where the comma ',' in $\mathbf{X}_{,i}$ denotes the partial derivative. The derivatives of base vectors with respect to coordinates can be expressed by the Christoffel symbols Γ_{ij}^k and Γ_{ijk} as

$$\mathbf{g}_{j,i} = \Gamma_{ij}^k \mathbf{g}_k = \Gamma_{ijk} \mathbf{g}^k, \quad \mathbf{g}_{,j}^i = -\Gamma_{jp}^i \mathbf{g}^p, \tag{3}$$

which provides the relations between the Christoffel symbols and components of the metric tensor as

$$\Gamma_{ijk} = g_{kl} \Gamma_{ij}^l = \tfrac{1}{2}\left(g_{ik,j} + g_{jk,i} - g_{ij,k}\right), \quad \Gamma_{ij}^p = g^{kp} \Gamma_{ijk}. \tag{4}$$

Furthermore, the partial derivative of an arbitrary vector $\mathbf{F}$ in the curvilinear coordinate system is

$$\frac{\partial \mathbf{F}}{\partial \xi^j} = F_{;j}^i \mathbf{g}_i = F_{i;j} \mathbf{g}^i, \tag{5}$$

where the semicolon ';' in $F_{;j}^i$ and $F_{i;j}$ represents the spatial covariant derivative, defined as follows:

$$F_{;j}^i = F_{,j}^i + F^m \Gamma_{jm}^i, \quad F_{i;j} = F_{i,j} - F_m \Gamma_{ji}^m. \tag{6}$$

On the other hand, for each point of the *mid-surface* Ω_0 characterized by the position vector $\boldsymbol{\rho}$, we define the natural (or covariant) base vectors $\boldsymbol{\rho}_\alpha$, dual (or contravariant) base vectors $\boldsymbol{\rho}^\alpha$, unit vector $\mathbf{n}$ normal to Ω_0, coefficients $a_{\alpha\beta}$ and $b_{\alpha\beta}$ of the first and second fundamental forms of the mid-surface and other quantities that will be used in this paper as

$$\begin{aligned} &\boldsymbol{\rho}_\alpha = \frac{\partial \boldsymbol{\rho}}{\partial \xi^\alpha} = \boldsymbol{\rho}_{,\alpha}, \quad (\alpha = 1, 2), \quad \mathbf{n} = \frac{\boldsymbol{\rho}_1 \times \boldsymbol{\rho}_2}{|\boldsymbol{\rho}_1 \times \boldsymbol{\rho}_2|}, \\ &\boldsymbol{\rho}_\alpha \cdot \boldsymbol{\rho}^\beta = \delta_\alpha^\beta, \quad a_{\alpha\beta} = \boldsymbol{\rho}_\alpha \cdot \boldsymbol{\rho}_\beta, \quad a^{\alpha\beta} = \boldsymbol{\rho}^\alpha \cdot \boldsymbol{\rho}^\beta, \\ &b_{\alpha\beta} = b_{\beta\alpha} = \mathbf{n} \cdot \boldsymbol{\rho}_{\alpha,\beta} = -\mathbf{n}_{,\beta} \cdot \boldsymbol{\rho}_\alpha, \quad b_\alpha^\beta = a^{\gamma\beta} b_{\alpha\gamma}, \end{aligned} \tag{7}$$

where the partial derivative $\mathbf{n}_{,\beta}$ is defined, based on the Weingarten formula, as

$$\mathbf{n}_{,\beta} = -b_\beta^\alpha \boldsymbol{\rho}_\alpha = -b_{\alpha\beta} \boldsymbol{\rho}^\alpha. \tag{8}$$

According to Eq. (1), $(2)_1$, $(7)_1$ and (8), the relations between the 3-D base vectors and those of the mid-surface are

$$\mathbf{g}_\alpha = \boldsymbol{\rho}_\alpha + \xi^3 \mathbf{n}_{,\alpha} = \left(\delta_\alpha^\omega - \xi^3 b_\alpha^\omega\right) \boldsymbol{\rho}_\omega, \quad \mathbf{g}_3 = \mathbf{n}, \tag{9}$$

which leads to the components g_{ij} of the metric tensor and the coefficients $d_{\alpha\beta}$ of the second fundamental form of the parallel surface Ω_p as

$$\begin{aligned} &g_{\alpha\beta} = \left(\delta_\alpha^\omega - \xi^3 b_\alpha^\omega\right)\left(\delta_\beta^\lambda - \xi^3 b_\beta^\lambda\right) a_{\omega\lambda}, \quad g_{\alpha 3} = 0, \quad g_{33} = 1, \\ &d_{\alpha\beta} = -\mathbf{n}_{,\beta} \cdot \mathbf{g}_\alpha = b_{\omega\beta}\left(\delta_\alpha^\omega - \xi^3 b_\alpha^\omega\right). \end{aligned} \tag{10}$$

If the parametric curves ξ^1 and ξ^2 are chosen to be the lines of curvatures of the shell body, the coordinate system will be referred to as the orthogonal parallel curvilinear coordinate system, where the unified finite shell elements with geometrical nonlinearity are formulated in this work. For this system, the three covariant basis vectors $\mathbf{g}_i$ are thus orthogonal to each other, which also holds for contravariant basis vectors $\mathbf{g}^i$. Their moduli (or length) are defined as

$$|\mathbf{g}_i| = H_i, \quad \left|\mathbf{g}^i\right| = 1/H_i, \quad (i = 1, 2, 3)\,, \tag{11}$$

where H_i are the Lamé parameters of the parallel surface Ω_p. The components g_{ij} and g^{ij} of the 3-D metric tensor become

$$\begin{aligned} &g_{ij} = g^{ij} = 0, \quad (i \neq j), \\ &g_{11} = 1/g^{11} = H_1^2, \quad g_{22} = 1/g^{22} = H_2^2, \quad g_{33} = 1/g^{33} = H_3^2 = 1. \end{aligned} \tag{12}$$

Substituting Eq. (12) into Eq. (4) yields Γ_{ij}^p in the orthogonal curvilinear coordinate system as

$$\begin{aligned} &\Gamma_{ij}^k = 0, \quad (i \neq j \neq k)\,, \\ &\Gamma_{ij}^i = \frac{1}{H_i}\frac{\partial H_i}{\partial \xi^j}, \quad (i \neq j \text{ or } i = j)\,, \\ &\Gamma_{ii}^j = -\frac{H_i}{H_j^2}\frac{\partial H_i}{\partial \xi^j}, \quad (i \neq j)\,. \end{aligned} \tag{13}$$

In addition, the coefficients $a_{\alpha\beta}$ and $b_{\alpha\beta}$ of the first and second fundamental forms and the components b_α^β of the mid-surface Ω_0 degenerate to

$$\begin{aligned} &a_{11} = A^2, \quad a_{12} = 0, \quad a_{22} = B^2, \\ &b_{11} = -A^2/R_1, \quad b_{12} = 0, \quad b_{22} = -B^2/R_2, \\ &b_1^1 = -1/R_1, \quad b_1^2 = b_2^1 = 0, \quad b_2^2 = -1/R_2, \end{aligned} \tag{14}$$

where A and B are the Lamé parameters of the mid-surface Ω_0; R_1 and R_2 are its principal curvature radii. Inserting Eq. (14) into Eq. (10), we have

$$\begin{aligned} &g_{11} = A^2\big(1 + \xi^3/R_1\big)^2, \quad g_{22} = B^2\big(1 + \xi^3/R_2\big)^2, \\ &d_{11} = -\frac{A^2}{R_1}\left(1 + \xi^3/R_1\right), \quad d_{12} = 0, \quad d_{22} = -\frac{B^2}{R_2}\left(1 + \xi^3/R_2\right), \end{aligned} \tag{15}$$

which results in the Lamé parameters H_i and principal curvature radii $\tilde{R}_\alpha$ of the parallel surface as

$$\begin{aligned} &H_1 = A\left(1 + \xi^3/R_1\right), \quad H_2 = B\left(1 + \xi^3/R_2\right), \quad H_3 = 1, \\ &1/\tilde{R}_1 = -d_{11}/g_{11} = 1/(R_1 + \xi^3), \quad 1/\tilde{R}_2 = -d_{22}/g_{22} = 1/(R_2 + \xi^3). \end{aligned} \tag{16}$$

In the orthogonal coordinate system, the infinitesimal in-plane area $\mathrm{d}\tilde{\mathbf{S}}$ on the parallel surface Ω_p and the infinitesimal volume $\mathrm{d}V$ of the shell structure $\mathcal{B}_r$ can be expressed as:

$$\mathrm{d}\tilde{\mathbf{S}} = H_1 H_2 d\xi^1 \mathrm{d}\xi^2 \mathbf{n} = H_1 H_2 \mathrm{d}\mathbf{S}/(AB), \quad \mathrm{d}V = H_1 H_2 H_3 \mathrm{d}\xi^1 \mathrm{d}\xi^2 \mathrm{d}\xi^3, \tag{17}$$

where $\mathrm{d}\mathbf{S} = AB\mathrm{d}\xi^1 \mathrm{d}\xi^2 \mathbf{n}$ is the infinitesimal in-plane area on the mid-surface Ω_0 of the shell.

2.2 Geometrical relations in the orthogonal curvilinear coordinate system

For highly flexible shell structures prone to suffering large displacements/rotations, post-buckling and even snapping, it is extremely vital to take account of the high-order terms of finite displacement derivatives into the geometrical relations so as to accurately predict the geometrically nonlinear response and the stress field distributions. Consider the motion $\mathbf{x} = \boldsymbol{\chi}(\mathbf{X}, t)$ of the shell body from the reference configuration $\mathcal{B}_r$ to the current configuration $\mathcal{B}_t$, where $\boldsymbol{\chi}$ is a vector function with a sufficiently regular property. The current position vector of the material point associated with $\mathbf{X}$ is given by $\mathbf{x}$. In the *total Lagrangian* description, we have the displacement vector $\mathbf{u}$ as

$$\mathbf{u} = \mathbf{x} - \mathbf{X} = u_i \mathbf{g}^i = u^i \mathbf{g}_i, \tag{18}$$

in which the last two equalities are in component forms described in the reference configuration $\mathcal{B}_r$. Thus, the deformation gradient tensor $\mathbf{F} = \nabla \mathbf{x}$ and the Green-Lagrange strain tensor $\mathbf{E} = \left(\mathbf{F}^{\mathrm{T}}\mathbf{F} - \mathbf{I}\right)/2$ as a measure of the strain satisfy

$$\mathbf{F} = \mathbf{I} + \nabla \mathbf{u}, \quad \mathbf{E} = \mathbf{E}_l + \mathbf{E}_{nl} = \frac{1}{2}\left[\nabla \mathbf{u} + (\nabla \mathbf{u})^{\mathrm{T}} + (\nabla \mathbf{u})^{\mathrm{T}} \cdot \nabla \mathbf{u}\right], \tag{19}$$

where the symbol ∇ denotes the gradient operator with respect to the reference configuration $\mathcal{B}_r$ with the displacement gradient being defined as $\nabla \mathbf{u} = \frac{\partial \mathbf{u}}{\partial \xi^j} \otimes \mathbf{g}^j$, and the superscript 'T' signifies the transpose. According to Eqs. (5) and (6), the linear part $\mathbf{E}_l$ and nonlinear part $\mathbf{E}_{nl}$ of the strain $\mathbf{E}$ in Eq. (19) can be derived as

$$\mathbf{E}_l = \frac{1}{2}\left[\nabla \mathbf{u} + (\nabla \mathbf{u})^{\mathrm{T}}\right] = \frac{1}{2}\left(u_{i;j} + u_{j;i}\right)\mathbf{g}^i \otimes \mathbf{g}^j = \frac{1}{2}\left(u_{j,i} + u_{i,j} - 2u_m \Gamma_{ij}^m\right)\mathbf{g}^i \otimes \mathbf{g}^j, \tag{20}$$

and

$$\mathbf{E}_{nl} = \frac{1}{2}(\nabla \mathbf{u})^{\mathrm{T}} \cdot \nabla \mathbf{u} = \frac{1}{2} u_{k;i} u_{;j}^k \mathbf{g}^i \otimes \mathbf{g}^j = \frac{1}{2}\left(u_{k,i} u_{,j}^k - u_m \Gamma_{ki}^m u_{,j}^k + u_{k,i} u^n \Gamma_{nj}^k - u_m \Gamma_{ki}^m u^n \Gamma_{nj}^k\right)\mathbf{g}^i \otimes \mathbf{g}^j, \tag{21}$$

where the symbol $\otimes$ is the dyad operator.

In the orthogonal curvilinear coordinate system, the covariant and contravariant basis vectors $\mathbf{g}_i$ and $\mathbf{g}^i$ are not necessarily unit vectors (see Eq. (11)). In order to facilitate the analysis of physical problems, we introduce a set of orthogonal normalization base vectors $\mathbf{e}_i$ as

$$\mathbf{e}_i = \mathbf{g}^i / \left|\mathbf{g}^i\right| = H_i \mathbf{g}^i = \mathbf{g}_i / \left|\mathbf{g}_i\right| = \mathbf{g}_i / H_i. \tag{22}$$

Furthermore, the displacement vector can be written, in terms of $\mathbf{e}_i$, as

$$\mathbf{u} = \tilde{u}_i \mathbf{e}_i, \tag{23}$$

where $\tilde{u}_i$ represent the *physical* components that are different from the *tensor* components u_i and u^i. In fact, using Eqs. (18), (22) and (23), we have

$$u_i = H_i \tilde{u}_i, \quad u^i = \tilde{u}_i / H_i. \tag{24}$$

Thus, substituting Eqs. (22) and (24) into Eqs. (20) and (21) yields

$$\begin{aligned}
\mathbf{E}_l &= \frac{1}{2}\sum_{i,j=1}^{3}\left[\left(\frac{\partial H_j}{\partial \xi^i}\tilde{u}_j + H_j\frac{\partial \tilde{u}_j}{\partial \xi^i} + \frac{\partial H_i}{\partial \xi^j}\tilde{u}_i + H_i\frac{\partial \tilde{u}_i}{\partial \xi^j}\right)\frac{\mathbf{e}_i}{H_i} \otimes \frac{\mathbf{e}_j}{H_j}\right] - \sum_{i,j,m=1}^{3}\left(H_m \tilde{u}_m \Gamma_{ij}^m \frac{\mathbf{e}_i}{H_i} \otimes \frac{\mathbf{e}_j}{H_j}\right), \\
\mathbf{E}_{nl} &= \frac{1}{2}\left\{\sum_{i,j,k=1}^{3}\left[\frac{\partial (H_k \tilde{u}_k)}{\partial \xi^i}\frac{\partial (\tilde{u}_k / H_k)}{\partial \xi^j}\frac{\mathbf{e}_i}{H_i} \otimes \frac{\mathbf{e}_j}{H_j}\right] - \sum_{i,j,k,m=1}^{3}\left[H_m \tilde{u}_m \Gamma_{ki}^m \frac{\partial (\tilde{u}_k / H_k)}{\partial \xi^j}\frac{\mathbf{e}_i}{H_i} \otimes \frac{\mathbf{e}_j}{H_j}\right]\right. \\
&\quad \left. + \sum_{i,j,k,n=1}^{3}\left[\frac{\partial (H_k \tilde{u}_k)}{\partial \xi^i}\frac{\tilde{u}_n}{H_n}\Gamma_{nj}^k \frac{\mathbf{e}_i}{H_i} \otimes \frac{\mathbf{e}_j}{H_j}\right] - \sum_{i,j,k,n,m=1}^{3}\left(H_m \tilde{u}_m \Gamma_{ki}^m \frac{\tilde{u}_n}{H_n}\Gamma_{nj}^k \frac{\mathbf{e}_i}{H_i} \otimes \frac{\mathbf{e}_j}{H_j}\right)\right\}.
\end{aligned} \tag{25}$$

In the present work, we only consider the shells with *constant* curvatures (e.g., cylindrical and spherical shells), which gives constant principal curvature radii R_1 and R_2. Moreover, if the in-plane curvilinear coordinates ξ^1 and ξ^2 are chosen to be the *arc-length coordinates*, the Lamé parameters A and B of the mid-surface Ω_0 fulfill $A = B = 1$. As a result, the derivatives of H_i with respect to ξ^1 and ξ^2 vanish according to Eq. (16), and $\partial H_\alpha/\partial\xi^3 = 1/R_\alpha$ ($\alpha = 1, 2$). Using Eqs. (13) and (16) and making the following variable substitutions:

$$(\alpha, \beta, z) \to \left(\xi^1, \xi^2, \xi^3\right), \quad (u_\alpha, u_\beta, u_z) \to (\tilde{u}_1, \tilde{u}_2, \tilde{u}_3), \quad (H_\alpha, H_\beta, H_z, R_\alpha, R_\beta) \to (H_1, H_2, H_3, R_1, R_2), \tag{26}$$

Eqs. $(19)_2$ and (25) can be derived and rearranged in matrix form as

$$\mathbf{E} = \mathbf{E}_l + \mathbf{E}_{nl} = (\mathbf{b}_l + \mathbf{b}_{nl})\mathbf{u}, \tag{27}$$

where $\mathbf{u}$ and $\mathbf{E}$ are now the 3-D displacement vector and the Green-Lagrange strain vector, respectively, which are defined as

$$\mathbf{u}(\alpha, \beta, z) = \left\{ \begin{array}{ccc} u_\alpha & u_\beta & u_z \end{array} \right\}^{\mathrm{T}}, \quad \mathbf{E} = \left\{ \begin{array}{cccccc} E_{\alpha\alpha} & E_{\beta\beta} & E_{zz} & E_{\alpha z} & E_{\beta z} & E_{\alpha\beta} \end{array} \right\}^{\mathrm{T}}, \tag{28}$$

The 6×3 linear and nonlinear differential operators $\mathbf{b}_l$ and $\mathbf{b}_{nl}$ in Eq. (27) are given by:

$$\mathbf{b}_l = \begin{bmatrix} \frac{\partial_\alpha}{H_\alpha} & 0 & \frac{1}{H_\alpha R_\alpha} \\ 0 & \frac{\partial_\beta}{H_\beta} & \frac{1}{H_\beta R_\beta} \\ 0 & 0 & \partial_z \\ \partial_z - \frac{1}{H_\alpha R_\alpha} & 0 & \frac{\partial_\alpha}{H_\alpha} \\ 0 & \partial_z - \frac{1}{H_\beta R_\beta} & \frac{\partial_\beta}{H_\beta} \\ \frac{\partial_\beta}{H_\beta} & \frac{\partial_\alpha}{H_\alpha} & 0 \end{bmatrix}, \tag{29}$$

and

$$\mathbf{b}_{nl} = \begin{bmatrix} \frac{1}{2H_\alpha^2}\left[(\partial_\alpha)^2 + \frac{2u_z\partial_\alpha}{R_\alpha} + \frac{u_\alpha}{R_\alpha^2}\right] & \frac{(\partial_\alpha)^2}{2H_\alpha^2} & \frac{1}{2H_\alpha^2}\left[(\partial_\alpha)^2 - \frac{2u_\alpha\partial_\alpha}{R_\alpha} + \frac{u_z}{R_\alpha^2}\right] \\ \frac{(\partial_\beta)^2}{2H_\beta^2} & \frac{1}{2H_\beta^2}\left[(\partial_\beta)^2 + \frac{2u_z\partial_\beta}{R_\beta} + \frac{u_\beta}{R_\beta^2}\right] & \frac{1}{2H_\beta^2}\left[(\partial_\beta)^2 - \frac{2u_\beta\partial_\beta}{R_\beta} + \frac{u_z}{R_\beta^2}\right] \\ \frac{1}{2}(\partial_z)^2 & \frac{1}{2}(\partial_z)^2 & \frac{1}{2}(\partial_z)^2 \\ \frac{1}{H_\alpha}\left(\partial_\alpha\partial_z + \frac{u_z\partial_z}{R_\alpha}\right) & \frac{\partial_\alpha\partial_z}{H_\alpha} & \frac{1}{H_\alpha}\left(\partial_\alpha\partial_z - \frac{u_\alpha\partial_z}{R_\alpha}\right) \\ \frac{\partial_\beta\partial_z}{H_\beta} & \frac{1}{H_\beta}\left(\partial_\beta\partial_z + \frac{u_z\partial_z}{R_\beta}\right) & \frac{1}{H_\beta}\left(\partial_\beta\partial_z - \frac{u_\beta\partial_z}{R_\beta}\right) \\ \frac{1}{H_\alpha H_\beta}\left(\partial_\alpha\partial_\beta + \frac{u_z\partial_\beta}{R_\alpha} + \frac{u_\beta}{R_\alpha R_\beta}\right) & \frac{1}{H_\alpha H_\beta}\left(\partial_\alpha\partial_\beta + \frac{u_z\partial_\alpha}{R_\beta}\right) & \frac{1}{H_\alpha H_\beta}\left(\partial_\alpha\partial_\beta - \frac{u_\alpha\partial_\beta}{R_\alpha} - \frac{u_\beta\partial_\alpha}{R_\beta}\right) \end{bmatrix}, \tag{30}$$

in which $\partial_\alpha = \partial(\cdot)/\partial\alpha$, $\partial_\beta = \partial(\cdot)/\partial\beta$, and $\partial_z = \partial(\cdot)/\partial z$. For the plate case, we have $R_\alpha \to \infty$, $R_\beta \to \infty$ and $H_\alpha = H_\beta = 1$, which make the differential operator matrices (29) and (30) degenerate to those in the Cartesian coordinate system [42].

2.3 Constitutive equations

In the total Lagrangian description, the Green-Lagrange strain vector $\mathbf{E}$ is work-conjugate to the second Piola-Kirchhoff stress vector $\mathbf{S}$, which is defined as $\mathbf{S} = \{S_{\alpha\alpha}, S_{\beta\beta}, S_{zz}, S_{\alpha z}, S_{\beta z}, S_{\alpha\beta}\}^{\mathrm{T}}$. In this work, we

assume that the shell response remains in the elastic regime without elasto-plastic behavior. Furthermore, the constitutive relation between $\mathbf{S}$ and $\mathbf{E}$ is assumed to be linear, i.e.

$$\mathbf{S} = \tilde{\mathbf{C}}\mathbf{E}, \tag{31}$$

where $\tilde{\mathbf{C}}$ is the material elastic matrix that is independent of the shell deformation. For homogeneous shell structures, $\tilde{\mathbf{C}}$ is constant. However, $\tilde{\mathbf{C}}$ will be a function of $\mathbf{X}$ for the non-homogeneous case such as composites.

The material elastic matrix $\tilde{\mathbf{C}}$ can be obtained by transforming its original form $\mathbf{C}$ from the material coordinate system (1, 2, 3) to the global system (α, β, z). For materials with *monoclinic symmetry*, the original elastic matrix $\mathbf{C}$ in the material system reads:

$$\mathbf{C} = \begin{bmatrix} C_{11} & C_{12} & C_{13} & 0 & 0 & C_{16} \\ & C_{22} & C_{23} & 0 & 0 & C_{26} \\ & & C_{33} & 0 & 0 & C_{36} \\ & & & C_{44} & C_{45} & 0 \\ & & & & C_{55} & 0 \\ & \text{sym.} & & & & C_{66} \end{bmatrix}. \tag{32}$$

For *isotropic* metallic materials considered in this work, the Young's modulus E_Y and the Poisson's ratio ν determine the elements of the original elastic matrix $\mathbf{C}$, i.e., $C_{16} = C_{26} = C_{36} = C_{45} = 0$ and

$$\begin{aligned} C_{11} = C_{22} = C_{33} &= \frac{(1-\nu)E_Y}{(1+\nu)(1-2\nu)}, \\ C_{12} = C_{13} = C_{23} &= \frac{\nu\, E_Y}{(1+\nu)(1-2\nu)}, \\ C_{44} = C_{55} = C_{66} &= \frac{E_Y}{2(1+\nu)}. \end{aligned} \tag{33}$$

2.4 CUF and finite element approximation

According to the Carrera Unified Formulation (CUF) for the 2-D shell theory, the 3-D displacement field $\mathbf{u}(\alpha, \beta, z)$ of the shell structure can be expanded as a set of thickness functions depending only on the thickness coordinate z and the corresponding variables depending on the in-plane arc-length coordinates α and β. Specifically, we have

$$\mathbf{u}(\alpha, \beta, z) = F_\tau(z)\mathbf{u}_\tau(\alpha, \beta), \qquad \tau = 0, 1, \cdots, N, \tag{34}$$

where F_τ are the expansion functions of the thickness coordinate z, $\mathbf{u}_\tau$ is the *generalized* displacement vector depending on the in-plane coordinates α and β, N denotes the order of expansion in the thickness direction, and the summing convention with the repeated index τ is assumed. The choice of F_τ and N is arbitrary, and different base functions (e.g. Taylor Expansions, Lagrange Expansions, Hierarchical Legendre Expansions) of any order can be taken into account to model the displacement field of shell structures along the thickness. Thus, the type of F_τ determines the class of the 2-D CUF shell model that is to be adopted.

In this paper, we will consider the Lagrange polynomials as F_τ functions along the thickness direction. The resulting shell theories are known as Lagrange Expansion (LE) CUF shell models in the literature [5]. The LE CUF shell model uses only pure displacement components as primary unknowns and thus permits boundary conditions to be applied directly to these displacements. Details of Lagrange polynomials not directly related to the CUF can be found in the book [52] and are not presented here. For brevity, the considered shell theories are indicated by the acronym LDN, which represents the Lagrange expansion, Displacement-based theory with the order of expansion N. Specifically, the two-node linear (LD1), three-node quadratic (LD2), and four-node cubic (LD3) Lagrange expansion functions are employed along the thickness direction to formulate linear to higher-order kinematics CUF shell elements with geometrical nonlinearity.

For the sake of generality, the Finite Element Method (FEM) is used to discretize the shell structure in the α-β plane. Therefore, the generalized displacement vector $\mathbf{u}_\tau(\alpha,\beta)$ can be approximated as follows:

$$\mathbf{u}_\tau(\alpha,\beta) = N_i(\alpha,\beta)\mathbf{q}_{\tau i}, \qquad i = 1,2,\ldots,p+1, \tag{35}$$

where N_i is the i-th shape function, p denotes the order of the shape functions and the repeated index i indicates summation. The vector of the FE nodal parameters $\mathbf{q}_{\tau i}$ is defined as

$$\mathbf{q}_{\tau i} = \left\{ \begin{array}{ccc} q_{\alpha_{\tau i}} & q_{\beta_{\tau i}} & q_{z_{\tau i}} \end{array} \right\}^{\mathrm{T}}. \tag{36}$$

The specific expressions of the shape functions N_i are not displayed here, and they can be found in many reference books about FEMs, for instance in Bathe [52]. In this work, the classical 2-D nine-node quadratic FE (Q9) will be adopted for the shape function in the α-β plane. Note that the choice of the thickness expansion functions for various kinematics is completely independent of that of the shell FEs.

3 Nonlinear equilibrium equations and secant stiffness matrix

It is well-known that nonlinear static equilibrium equations can be easily derived by using the principle of virtual work, which states that for arbitrary infinitesimal virtual displacement satisfying the prescribed geometrical constraints, the virtual variation of internal strain energy (δL_{int}) must be equal to the virtual variation of the work of external loadings (δL_{ext}), i.e.,

$$\delta L_{\mathrm{int}} = \delta L_{\mathrm{ext}}, \tag{37}$$

where δ represents the virtual variation operator. The analysis of large displacement/rotation, post-buckling and snapping behaviors of elastic systems results in complex nonlinear differential problems which are difficult to solve analytically. However, based on the FEM (Eq. (35)) and CUF (Eq. (34)), the nonlinear equilibrium equation (37) of the shell structure can be expressed as a system of nonlinear algebraic equations which will be derived below and solved along with the proper numerical method.

For the total Lagrangian formulation, the work-conjugate vectors giving the virtual variation of the internal strain energy are the second Piola-Kirchhoff stress vector $\mathbf{S}$ and the variation of the Green-Lagrange strain vector $\delta\mathbf{E}$. Thus, we have

$$\delta L_{\mathrm{int}} = < \delta\mathbf{E}^{\mathrm{T}}\mathbf{S} >, \tag{38}$$

where $< (\cdot) >= \int_{\mathcal{B}_r}(\cdot)\,\mathrm{d}V$, $\mathcal{B}_r$ is the undeformed reference configuration of the shell body, and $\mathrm{d}V = H_\alpha H_\beta H_z \mathrm{d}\alpha\mathrm{d}\beta\mathrm{d}z$ is the infinitesimal initial volume of the shell structure in $\mathcal{B}_r$, which is defined in Eq. (17). According to Eqs. (34) and (35), the strain vector $\mathbf{E}$ in Eq. (27) and its virtual variation $\delta\mathbf{E}$ can be expressed in terms of the generalized FE nodal unknowns $\mathbf{q}_{\tau i}$ and $\delta\mathbf{q}_{sj}$ as

$$\mathbf{E} = (\mathbf{B}_l^{\tau i} + \mathbf{B}_{nl}^{\tau i})\mathbf{q}_{\tau i}, \qquad \delta\mathbf{E} = (\mathbf{B}_l^{sj} + 2\mathbf{B}_{nl}^{sj})\delta\mathbf{q}_{sj}, \tag{39}$$

where the two matrices $\mathbf{B}_l^{\tau i}$ and $\mathbf{B}_{nl}^{\tau i}$ of linear and nonlinear geometrical relations are given by

$$\mathbf{B}_l^{\tau i} = \mathbf{b}_l(F_\tau\, N_i) = \begin{bmatrix} \frac{F_\tau N_{i,\alpha}}{H_\alpha} & 0 & \frac{F_\tau N_i}{H_\alpha R_\alpha} \\ 0 & \frac{F_\tau N_{i,\beta}}{H_\beta} & \frac{F_\tau N_i}{H_\beta R_\beta} \\ 0 & 0 & F_{\tau,z}N_i \\ F_{\tau,z}N_i - \frac{F_\tau N_i}{H_\alpha R_\alpha} & 0 & \frac{F_\tau N_{i,\alpha}}{H_\alpha} \\ 0 & F_{\tau,z}N_i - \frac{F_\tau N_i}{H_\beta R_\beta} & \frac{F_\tau N_{i,\beta}}{H_\beta} \\ \frac{F_\tau N_{i,\beta}}{H_\beta} & \frac{F_\tau N_{i,\alpha}}{H_\alpha} & 0 \end{bmatrix}, \tag{40}$$

and

$$
\begin{aligned}
\mathbf{B}_{nl}^{\tau i}[1,1] &= \tfrac{1}{2H_\alpha^2}\left[\left(u_{\alpha,\alpha}+\tfrac{u_z}{R_\alpha}\right)F_\tau N_{i,\alpha}+\left(\tfrac{u_\alpha}{R_\alpha}-u_{z,\alpha}\right)\tfrac{F_\tau N_i}{R_\alpha}\right], \qquad \mathbf{B}_{nl}^{\tau i}[1,2]=\tfrac{u_{\beta,\alpha}F_\tau N_{i,\alpha}}{2H_\alpha^2},\\
\mathbf{B}_{nl}^{\tau i}[1,3] &= \tfrac{1}{2H_\alpha^2}\left[\left(u_{z,\alpha}-\tfrac{u_\alpha}{R_\alpha}\right)F_\tau N_{i,\alpha}+\left(u_{\alpha,\alpha}+\tfrac{u_z}{R_\alpha}\right)\tfrac{F_\tau N_i}{R_\alpha}\right], \qquad \mathbf{B}_{nl}^{\tau i}[2,1]=\tfrac{u_{\alpha,\beta}F_\tau N_{i,\beta}}{2H_\beta^2},\\
\mathbf{B}_{nl}^{\tau i}[2,2] &= \tfrac{1}{2H_\beta^2}\left[\left(u_{\beta,\beta}+\tfrac{u_z}{R_\beta}\right)F_\tau N_{i,\beta}+\left(\tfrac{u_\beta}{R_\beta}-u_{z,\beta}\right)\tfrac{F_\tau N_i}{R_\beta}\right], \qquad \mathbf{B}_{nl}^{\tau i}[3,1]=\tfrac{u_{\alpha,z}F_{\tau,z}N_i}{2},\\
\mathbf{B}_{nl}^{\tau i}[2,3] &= \tfrac{1}{2H_\beta^2}\left[\left(u_{z,\beta}-\tfrac{u_\beta}{R_\beta}\right)F_\tau N_{i,\beta}+\left(u_{\beta,\beta}+\tfrac{u_z}{R_\beta}\right)\tfrac{F_\tau N_i}{R_\beta}\right], \qquad \mathbf{B}_{nl}^{\tau i}[3,2]=\tfrac{u_{\beta,z}F_{\tau,z}N_i}{2},\\
\mathbf{B}_{nl}^{\tau i}[4,1] &= \tfrac{1}{2H_\alpha}\left[\left(u_{\alpha,\alpha}+\tfrac{u_z}{R_\alpha}\right)F_{\tau,z}N_i+u_{\alpha,z}F_\tau N_{i,\alpha}-\tfrac{u_{z,z}F_\tau N_i}{R_\alpha}\right], \quad \mathbf{B}_{nl}^{\tau i}[3,3]=\tfrac{u_{z,z}F_{\tau,z}N_i}{2},\\
\mathbf{B}_{nl}^{\tau i}[4,2] &= \tfrac{u_{\beta,\alpha}F_{\tau,z}N_i+u_{\beta,z}F_\tau N_{i,\alpha}}{2H_\alpha}, \quad \mathbf{B}_{nl}^{\tau i}[5,1]=\tfrac{u_{\alpha,\beta}F_{\tau,z}N_i+u_{\alpha,z}F_\tau N_{i,\beta}}{2H_\beta},\\
\mathbf{B}_{nl}^{\tau i}[4,3] &= \tfrac{1}{2H_\alpha}\left[\left(u_{z,\alpha}-\tfrac{u_\alpha}{R_\alpha}\right)F_{\tau,z}N_i+u_{z,z}F_\tau N_{i,\alpha}+\tfrac{u_{\alpha,z}F_\tau N_i}{R_\alpha}\right],\\
\mathbf{B}_{nl}^{\tau i}[5,2] &= \tfrac{1}{2H_\beta}\left[\left(u_{\beta,\beta}+\tfrac{u_z}{R_\beta}\right)F_{\tau,z}N_i+u_{\beta,z}F_\tau N_{i,\beta}-\tfrac{u_{z,z}F_\tau N_i}{R_\beta}\right],\\
\mathbf{B}_{nl}^{\tau i}[5,3] &= \tfrac{1}{2H_\beta}\left[\left(u_{z,\beta}-\tfrac{u_\beta}{R_\beta}\right)F_{\tau,z}N_i+u_{z,z}F_\tau N_{i,\beta}+\tfrac{u_{\beta,z}F_\tau N_i}{R_\beta}\right],\\
\mathbf{B}_{nl}^{\tau i}[6,1] &= \tfrac{1}{2H_\alpha H_\beta}\left[u_{\alpha,\beta}F_\tau N_{i,\alpha}+\left(u_{\alpha,\alpha}+\tfrac{u_z}{R_\alpha}\right)F_\tau N_{i,\beta}+\left(\tfrac{u_\beta}{R_\beta}-u_{z,\beta}\right)\tfrac{F_\tau N_i}{R_\alpha}\right],\\
\mathbf{B}_{nl}^{\tau i}[6,2] &= \tfrac{1}{2H_\alpha H_\beta}\left[\left(u_{\beta,\beta}+\tfrac{u_z}{R_\beta}\right)F_\tau N_{i,\alpha}+u_{\beta,\alpha}F_\tau N_{i,\beta}+\left(\tfrac{u_\alpha}{R_\alpha}-u_{z,\alpha}\right)\tfrac{F_\tau N_i}{R_\beta}\right],\\
\mathbf{B}_{nl}^{\tau i}[6,3] &= \tfrac{1}{2H_\alpha H_\beta}\left[\left(u_{z,\beta}-\tfrac{u_\beta}{R_\beta}\right)F_\tau N_{i,\alpha}+\left(u_{z,\alpha}-\tfrac{u_\alpha}{R_\alpha}\right)F_\tau N_{i,\beta}+\left(\tfrac{u_{\alpha,\beta}}{R_\alpha}+\tfrac{u_{\beta,\alpha}}{R_\beta}\right)F_\tau N_i\right],
\end{aligned}
\tag{41}
$$

in which the comma again denotes the partial derivative. Replacing the indices τ and i with s and j in Eqs. (40) and (41) leads to the other two matrices $\mathbf{B}_l^{sj}$ and $\mathbf{B}_{nl}^{sj}$.

Substituting the geometrical relation $(39)_2$ and the constitutive equation (31) into Eq. (38), we have

$$
\begin{aligned}
\delta L_{\text{int}} &= \delta\mathbf{q}_{sj}^{\mathrm{T}} < \left(\mathbf{B}_l^{sj}+2\,\mathbf{B}_{nl}^{sj}\right)^{\mathrm{T}}\tilde{\mathbf{C}}\left(\mathbf{B}_l^{\tau i}+\mathbf{B}_{nl}^{\tau i}\right) > \mathbf{q}_{\tau i}\\
&= \delta\mathbf{q}_{sj}^{\mathrm{T}}\,\mathbf{K}_0^{ij\tau s}\,\mathbf{q}_{\tau i}+\delta\mathbf{q}_{sj}^{\mathrm{T}}\,\mathbf{K}_{lnl}^{ij\tau s}\,\mathbf{q}_{\tau i}+\delta\mathbf{q}_{sj}^{\mathrm{T}}\,\mathbf{K}_{nll}^{ij\tau s}\,\mathbf{q}_{\tau i}+\delta\mathbf{q}_{sj}^{\mathrm{T}}\,\mathbf{K}_{nlnl}^{ij\tau s}\,\mathbf{q}_{\tau i}\\
&= \delta\mathbf{q}_{sj}^{\mathrm{T}}\,\mathbf{K}_S^{ij\tau s}\,\mathbf{q}_{\tau i},
\end{aligned}
\tag{42}
$$

where $\mathbf{K}_S^{ij\tau s}=\mathbf{K}_0^{ij\tau s}+\mathbf{K}_{lnl}^{ij\tau s}+\mathbf{K}_{nll}^{ij\tau s}+\mathbf{K}_{nlnl}^{ij\tau s}$ is the *Fundamental Nucleus* (FN) of the *secant* stiffness matrix. Note that $\mathbf{K}_0^{ij\tau s}$ (the linear stiffness matrix) stands for the linear component of $\mathbf{K}_S$, $\mathbf{K}_{lnl}^{ij\tau s}$ and $\mathbf{K}_{nll}^{ij\tau s}$ represent the nonlinear contributions of first order, and $\mathbf{K}_{nlnl}^{ij\tau s}$ contains the nonlinearities of second order [42, 45]. These 3×3 matrices are obviously defined as

$$
\begin{aligned}
\mathbf{K}_0^{ij\tau s} &=< (\mathbf{B}_l^{sj})^{\mathrm{T}}\tilde{\mathbf{C}}\,\mathbf{B}_l^{\tau i} > , \qquad \mathbf{K}_{lnl}^{ij\tau s} =< (\mathbf{B}_l^{sj})^{\mathrm{T}}\tilde{\mathbf{C}}\,\mathbf{B}_{nl}^{\tau i} >,\\
\mathbf{K}_{nll}^{ij\tau s} &= 2 < (\mathbf{B}_{nl}^{sj})^{\mathrm{T}}\tilde{\mathbf{C}}\,\mathbf{B}_l^{\tau i} > , \quad \mathbf{K}_{nlnl}^{ij\tau s} = 2 < (\mathbf{B}_{nl}^{sj})^{\mathrm{T}}\tilde{\mathbf{C}}\,\mathbf{B}_{nl}^{\tau i} >,
\end{aligned}
\tag{43}
$$

where the actual computations of these matrices $\mathbf{K}_0^{ij\tau s}$, $\mathbf{K}_{lnl}^{ij\tau s}$, $\mathbf{K}_{nll}^{ij\tau s}$, and $\mathbf{K}_{nlnl}^{ij\tau s}$ have been carried out directly in the FORTRAN program via the matrix multiplication after the two matrices $\mathbf{B}_l^{\tau i}$ and $\mathbf{B}_{nl}^{\tau i}$ are provided according to Eqs. (40) and (41).

If the thickness expansion functions ($F_\tau = F_s$ for $\tau = s$) and the in-plane shape functions ($N_i = N_j$ for $i = j$) are given, the element secant stiffness matrix of arbitrary refined shell models accounting for geometrical nonlinearity can be established by expanding the FN of the 3×3 secant stiffness matrix $\mathbf{K}_S^{ij\tau s}$

and looping the indices $\tau, s = 0, ..., N$ and $i, j = 1, ..., p+1$. Consequently, by properly selecting various shell kinematics (i.e., by choosing F_τ as well as the order of expansion N), the classical, higher-order and refined shell theories as well as the related secant stiffness matrix can be implemented in an automatic and unified manner based on the index notation of CUF, especially considering the effect of geometrical nonlinearity.

If we further insert Eq. (42) into the principle of virtual work (37) and formulate the virtual variation of the external work δL_{ext} by $\delta \mathbf{q}_{sj}$ (conservative systems are considered in this work), the nonlinear equilibrium conditions of the generic shell theory can be obtained in a simple and unified manner as

$$\mathbf{K}_S^{ij\tau s}\, \mathbf{q}_{\tau i} - \mathbf{p}_{sj} = \mathbf{0}, \tag{44}$$

which represents a set of three nonlinear algebraic equations, where $\mathbf{p}_{sj}$ is the FN of the nodal loading vector and its derivation is not presented in this paper, but can be found in [50].

Once the *element* secant stiffness matrix is obtained according to the desirable approximation order, it can be assembled in the classical way of FEM, see [5]. In fact, by conducting the finite element assembly procedure in the framework of CUF, we can obtain the nonlinear algebraic governing equations from Eq. (44) as

$$\mathbf{K}_S\, \mathbf{q} - \mathbf{p} = \mathbf{0}, \tag{45}$$

where $\mathbf{K}_S$, $\mathbf{q}$, and $\mathbf{p}$ are *global, assembled* FE arrays of the whole shell structure. For more details about the calculation of the work of external loadings and the associated vector of generalized forces $\mathbf{p}$, interested readers can be referred to Carrera *et al.* [5].

4 Linearization for tangent stiffness matrix

4.1 Newton-Raphson method with path-following constraint

For the purpose of conducting the finite element calculation of the nonlinear algebraic governing equations (45), an incremental linearized scheme, typically the Newton-Raphson method (or tangent method), has been used to solve the fully geometrically nonlinear beam and plate systems [42, 45, 46, 47]. Based on the Newton-Raphson method [53], Eq. (45) can be rewritten as:

$$\boldsymbol{\varphi}_{res} \equiv \mathbf{K}_S\, \mathbf{q} - \mathbf{p} = \mathbf{0}, \tag{46}$$

where $\boldsymbol{\varphi}_{res}$ is the vector of the *residual nodal forces* (unbalanced nodal force vector). Expanding $\boldsymbol{\varphi}_{res}$ of Eq. (46) in Taylor's series about a known solution $(\mathbf{q}, \mathbf{p})$, utilizing the linearization method and omitting the higher-order terms, we have

$$\boldsymbol{\varphi}_{res}(\mathbf{q} + \delta\mathbf{q}, \mathbf{p} + \delta\mathbf{p}) = \boldsymbol{\varphi}_{res}(\mathbf{q}, \mathbf{p}) + \frac{\partial \boldsymbol{\varphi}_{res}}{\partial \mathbf{q}}\, \delta\mathbf{q} + \frac{\partial \boldsymbol{\varphi}_{res}}{\partial \mathbf{p}}\, \delta\lambda\, \mathbf{p}_{ref} = \mathbf{0}, \tag{47}$$

where $\partial\boldsymbol{\varphi}_{res}/\partial\mathbf{q} = \mathbf{K}_T$ is the *tangent* stiffness matrix that will be derived in the next subsection and $-\partial\boldsymbol{\varphi}_{res}/\partial\mathbf{p}$ is equal to the unit matrix $\mathbf{I}$. In Eq. (47), it has been assumed that the load varies directly with the vector of the reference loading $\mathbf{p}_{ref}$ with a rate of change equal to the load parameter λ, i.e. $\mathbf{p} = \lambda\, \mathbf{p}_{ref}$. It should be emphasized that, since we take the load-scaling parameter λ as a variable, an additional constraint relationship $c(\delta\mathbf{q}, \delta\lambda)$ is required to Eq. (47), which finally gives

$$\begin{cases} \mathbf{K}_T\, \delta\mathbf{q} = \delta\lambda\, \mathbf{p}_{ref} - \boldsymbol{\varphi}_{res}, \\ c(\delta\mathbf{q}, \delta\lambda) = 0. \end{cases} \tag{48}$$

In terms of the characteristics of the constraint equation $(48)_2$, different incremental schemes can be implemented. In this work, a path-following constraint equation, which is a function of both displacement and load parameter variations, will be utilized. Specifically, an arc-length method proposed by Crisfield [54, 55] and later modified by Carrera [56] is exploited, where the constraint relationship corresponds to a multi-dimensional sphere with radius equal to the given arc-length value that varies at each load step

depending on the ratio of convergence at the previous iteration. More information about the arc-length method is referred to the above-mentioned literature.

In this work, due to the generally non-symmetric behaviour of the secant stiffness matrix, we will employ the tangent stiffness matrix to formulate the linearized iterative scheme while the secant stiffness matrix is used merely for evaluating the residual $\boldsymbol{\varphi}_{res}$ at each iteration. Furthermore, the *full* Newton-Raphson method that updates the tangent stiffness matrix at each iteration will be used to conduct the numerical calculations. For more detailed discussions on these aspects, the interested readers are referred to the paper of Pagani and Carrera [45] as well as the references cited therein.

4.2 Fundamental nucleus of tangent stiffness matrix

Note that the FN of the tangent stiffness matrix $\mathbf{K}_T$ can be obtained from the linearization of the nonlinear equilibrium equation [57], see Eq. (47). For the conservative loading, the linearization of the virtual variation of external loads vanishes, i.e. $\mathrm{d}(\delta L_{\mathrm{ext}}) = 0$, where the symbol 'd' stands for the linearized differential operator. After linearizing the virtual variation of the internal strain energy, we can derive the tangent stiffness matrix as

$$\mathrm{d}(\delta L_{\mathrm{int}}) = < \mathrm{d}(\delta \mathbf{E}^{\mathrm{T}}\mathbf{S}) > = < \delta \mathbf{E}^{\mathrm{T}}\mathrm{d}\mathbf{S} > + < \mathrm{d}(\delta \mathbf{E}^{\mathrm{T}})\mathbf{S} > = \delta \mathbf{q}_{sj}^{\mathrm{T}} \mathbf{K}_T^{ij\tau s} \mathrm{d}\mathbf{q}_{\tau i}, \tag{49}$$

where $\mathbf{K}_T^{ij\tau s} = \mathbf{K}_0^{ij\tau s} + \mathbf{K}_{T_1}^{ij\tau s} + \mathbf{K}_{\sigma}^{ij\tau s}$ is the FN of the tangent stiffness matrix. Thus, the only terms to be linearized are the stress-strain constitutive equation and the strain-displacement geometrical relation. We will separately consider each nonlinear contribution $\mathbf{K}_{T_1}^{ij\tau s}$ and $\mathbf{K}_{\sigma}^{ij\tau s}$ below.

The first term $< \delta \mathbf{E}^{\mathrm{T}}\mathrm{d}\mathbf{S} >$ in Eq. (49) can be derived by linearizing the constitutive equation (31). Specifically, using the differential symbol 'd' to replace the variation symbol δ in Eq. $(39)_2$ and under the assumption of constant material coefficients (i.e., $\mathrm{d}\tilde{\mathbf{C}} = 0$), we have

$$\mathrm{d}\mathbf{S} = \mathrm{d}(\tilde{\mathbf{C}}\mathbf{E}) = \tilde{\mathbf{C}}\mathrm{d}\mathbf{E} = \tilde{\mathbf{C}}(\mathbf{B}_l^{\tau i} + 2\,\mathbf{B}_{nl}^{\tau i})\mathrm{d}\mathbf{q}_{\tau i}, \tag{50}$$

which, combined with Eq. $(39)_2$ and (43), leads to

$$\begin{aligned} < \delta \mathbf{E}^{\mathrm{T}}\mathrm{d}\mathbf{S} > &= \delta \mathbf{q}_{sj}^{\mathrm{T}} < (\mathbf{B}_l^{sj} + 2\,\mathbf{B}_{nl}^{sj})^{\mathrm{T}} \tilde{\mathbf{C}}\, (\mathbf{B}_l^{\tau i} + 2\,\mathbf{B}_{nl}^{\tau i}) > \mathrm{d}\mathbf{q}_{\tau i} \\ &= \delta \mathbf{q}_{sj}^{\mathrm{T}}\, \mathbf{K}_0^{ij\tau s} \mathrm{d}\mathbf{q}_{\tau i} + \delta \mathbf{q}_{sj}^{\mathrm{T}} \left(2\,\mathbf{K}_{lnl}^{ij\tau s}\right) \mathrm{d}\mathbf{q}_{\tau i} + \delta \mathbf{q}_{sj}^{\mathrm{T}}\, \mathbf{K}_{nll}^{ij\tau s} \mathrm{d}\mathbf{q}_{\tau i} + \delta \mathbf{q}_{sj}^{\mathrm{T}} \left(2\,\mathbf{K}_{nlnl}^{ij\tau s}\right) \mathrm{d}\mathbf{q}_{\tau i} \\ &= \delta \mathbf{q}_{sj}^{\mathrm{T}} \left(\mathbf{K}_0^{ij\tau s} + \mathbf{K}_{T_1}^{ij\tau s}\right) \mathrm{d}\mathbf{q}_{\tau i}, \end{aligned} \tag{51}$$

where $\mathbf{K}_{T_1}^{ij\tau s} = 2\,\mathbf{K}_{lnl}^{ij\tau s} + \mathbf{K}_{nll}^{ij\tau s} + 2\,\mathbf{K}_{nlnl}^{ij\tau s}$ is the nonlinear contribution to $\mathbf{K}_T^{ij\tau s}$ resulting from the linearization of the constitutive relation. Note that $\mathbf{K}_0^{ij\tau s}$, $\mathbf{K}_{lnl}^{ij\tau s}$, $\mathbf{K}_{nll}^{ij\tau s}$, and $\mathbf{K}_{nlnl}^{ij\tau s}$ are the same 3×3 FNs as presented in Eq. (43).

The derivation of the second integration term $< \mathrm{d}(\delta \mathbf{E}^{\mathrm{T}})\mathbf{S} >$ in Eq. (49) demands for conducting the linearization of the nonlinear geometrical relation. Thus, following Crisfield [58] and based on Eqs. (27)-(30), we have the components of the 6×1 vector $\mathrm{d}(\delta \mathbf{E})$ as

$$\begin{aligned} \mathrm{d}(\delta \mathbf{E})[1,1] &= \tfrac{1}{H_\alpha^2}\Big[\mathrm{d}u_{\alpha,\alpha}\delta u_{\alpha,\alpha} + \tfrac{\mathrm{d}u_\alpha \delta u_\alpha}{R_\alpha^2} + \mathrm{d}u_{\beta,\alpha}\delta u_{\beta,\alpha} + \mathrm{d}u_{z,\alpha}\delta u_{z,\alpha} + \tfrac{\mathrm{d}u_z \delta u_z}{R_\alpha^2} \\ &+ \tfrac{1}{R_\alpha}\left(\mathrm{d}u_z \delta u_{\alpha,\alpha} - \mathrm{d}u_{z,\alpha}\delta u_\alpha + \mathrm{d}u_{\alpha,\alpha}\delta u_z - \mathrm{d}u_\alpha \delta u_{z,\alpha}\right)\Big], \\ \mathrm{d}(\delta \mathbf{E})[2,1] &= \tfrac{1}{H_\beta^2}\Big[\mathrm{d}u_{\alpha,\beta}\delta u_{\alpha,\beta} + \mathrm{d}u_{\beta,\beta}\delta u_{\beta,\beta} + \tfrac{\mathrm{d}u_\beta \delta u_\beta}{R_\beta^2} + \mathrm{d}u_{z,\beta}\delta u_{z,\beta} + \tfrac{\mathrm{d}u_z \delta u_z}{R_\beta^2} \\ &+ \tfrac{1}{R_\beta}\left(\mathrm{d}u_z \delta u_{\beta,\beta} - \mathrm{d}u_{z,\beta}\delta u_\beta + \mathrm{d}u_{\beta,\beta}\delta u_z - \mathrm{d}u_\beta \delta u_{z,\beta}\right)\Big], \\ \mathrm{d}(\delta \mathbf{E})[3,1] &= \mathrm{d}u_{\alpha,z}\delta u_{\alpha,z} + \mathrm{d}u_{\beta,z}\delta u_{\beta,z} + \mathrm{d}u_{z,z}\delta u_{z,z}, \end{aligned} \tag{52}$$

and

$$
\begin{aligned}
\mathrm{d}(\delta\mathbf{E})[4,1] &= \tfrac{1}{H_\alpha}\Big[\mathrm{d}u_{\alpha,\alpha}\delta u_{\alpha,z}+\mathrm{d}u_{\alpha,z}\delta u_{\alpha,\alpha}+\mathrm{d}u_{\beta,\alpha}\delta u_{\beta,z}+\mathrm{d}u_{\beta,z}\delta u_{\beta,\alpha}+\mathrm{d}u_{z,\alpha}\delta u_{z,z}+\mathrm{d}u_{z,z}\delta u_{z,\alpha}\\
&+ \tfrac{1}{R_\alpha}\left(\mathrm{d}u_z\delta u_{\alpha,z}-\mathrm{d}u_{z,z}\delta u_\alpha+\mathrm{d}u_{\alpha,z}\delta u_z-\mathrm{d}u_\alpha\delta u_{z,z}\right)\Big],\\
\mathrm{d}(\delta\mathbf{E})[5,1] &= \tfrac{1}{H_\beta}\Big[\mathrm{d}u_{\alpha,\beta}\delta u_{\alpha,z}+\mathrm{d}u_{\alpha,z}\delta u_{\alpha,\beta}+\mathrm{d}u_{\beta,\beta}\delta u_{\beta,z}+\mathrm{d}u_{\beta,z}\delta u_{\beta,\beta}+\mathrm{d}u_{z,\beta}\delta u_{z,z}+\mathrm{d}u_{z,z}\delta u_{z,\beta}\\
&+ \tfrac{1}{R_\beta}\left(\mathrm{d}u_z\delta u_{\beta,z}-\mathrm{d}u_{z,z}\delta u_\beta+\mathrm{d}u_{\beta,z}\delta u_z-\mathrm{d}u_\beta\delta u_{z,z}\right)\Big],\\
\mathrm{d}(\delta\mathbf{E})[6,1] &= \tfrac{1}{H_\alpha H_\beta}\Big[\mathrm{d}u_{\alpha,\alpha}\delta u_{\alpha,\beta}+\mathrm{d}u_{\alpha,\beta}\delta u_{\alpha,\alpha}+\mathrm{d}u_{\beta,\alpha}\delta u_{\beta,\beta}+\mathrm{d}u_{\beta,\beta}\delta u_{\beta,\alpha}+\mathrm{d}u_{z,\alpha}\delta u_{z,\beta}\\
&+ \mathrm{d}u_{z,\beta}\delta u_{z,\alpha}+\tfrac{1}{R_\alpha R_\beta}\left(\mathrm{d}u_\beta\delta u_\alpha+\mathrm{d}u_\alpha\delta u_\beta\right)+\tfrac{1}{R_\alpha}(\mathrm{d}u_z\delta u_{\alpha,\beta}-\mathrm{d}u_{z,\beta}\delta u_\alpha+\mathrm{d}u_{\alpha,\beta}\delta u_z\\
&- \mathrm{d}u_\alpha\delta u_{z,\beta})+\tfrac{1}{R_\beta}\left(\mathrm{d}u_z\delta u_{\beta,\alpha}-\mathrm{d}u_{z,\alpha}\delta u_\beta+\mathrm{d}u_{\beta,\alpha}\delta u_z-\mathrm{d}u_\beta\delta u_{z,\alpha}\right)\Big],
\end{aligned}
\tag{53}
$$

It should be emphasized that the relation $\mathrm{d}(\delta\mathbf{E}_l)=0$ has been used in deriving Eqs. (52) and (53). By employing the CUF (34) and the FE approximation (35) for both the linearized differential variables (i.e. $\mathrm{d}\mathbf{u}=F_\tau N_i\mathrm{d}\mathbf{q}_{\tau i}$) and the variations (i.e. $\delta\mathbf{u}=F_s N_j\delta\mathbf{q}_{sj}$), we can express the vector $\mathrm{d}(\delta\mathbf{E})$ in terms of F_τ, N_i, F_s and N_j. Substituting the resulting expression of $\mathrm{d}(\delta\mathbf{E})$ into the second integration term $<\mathrm{d}(\delta\mathbf{E}^{\mathrm{T}})\mathbf{S}>$, we can obtain

$$
\begin{aligned}
<\mathrm{d}(\delta\mathbf{E}^{\mathrm{T}})\mathbf{S}> &= \mathrm{d}(\delta\mathbf{E}^{\mathrm{T}})\Big(\mathbf{S}_l+\mathbf{S}_{nl}\Big) = \delta\mathbf{q}_{sj}^{\mathrm{T}}\mathbf{K}_\sigma^{ij\tau s}\mathrm{d}\mathbf{q}_{\tau i} = \delta\mathbf{q}_{sj}^{\mathrm{T}}\Big(\mathbf{K}_{\sigma_l}^{ij\tau s}+\mathbf{K}_{\sigma_{nl}}^{ij\tau s}\Big)\mathrm{d}\mathbf{q}_{\tau i}\\
&= \mathbf{K}_\sigma^{ij\tau s}[1,1]\,\delta q_{\alpha_{sj}}\mathrm{d}q_{\alpha_{\tau i}}+\mathbf{K}_\sigma^{ij\tau s}[2,2]\,\delta q_{\beta_{sj}}\mathrm{d}q_{\beta_{\tau i}}+\mathbf{K}_\sigma^{ij\tau s}[3,3]\,\delta q_{z_{sj}}\mathrm{d}q_{z_{\tau i}}\\
&+ \mathbf{K}_\sigma^{ij\tau s}[1,3]\,\delta q_{\alpha_{sj}}\mathrm{d}q_{z_{\tau i}}+\mathbf{K}_\sigma^{ij\tau s}[3,1]\,\delta q_{z_{sj}}\mathrm{d}q_{\alpha_{\tau i}}+\mathbf{K}_\sigma^{ij\tau s}[2,3]\,\delta q_{\beta_{sj}}\mathrm{d}q_{z_{\tau i}}\\
&+ \mathbf{K}_\sigma^{ij\tau s}[3,2]\,\delta q_{z_{sj}}\mathrm{d}q_{\beta_{\tau i}}+\mathbf{K}_\sigma^{ij\tau s}[1,2]\,\delta q_{\alpha_{sj}}\mathrm{d}q_{\beta_{\tau i}}+\mathbf{K}_\sigma^{ij\tau s}[2,1]\,\delta q_{\beta_{sj}}\mathrm{d}q_{\alpha_{\tau i}},
\end{aligned}
\tag{54}
$$

where $\mathbf{S}_l=\tilde{\mathbf{C}}\mathbf{E}_l$ and $\mathbf{S}_{nl}=\tilde{\mathbf{C}}\mathbf{E}_{nl}$ based on Eqs. (27) and (31), $\mathbf{K}_\sigma^{ij\tau s}=\mathbf{K}_{\sigma_l}^{ij\tau s}+\mathbf{K}_{\sigma_{nl}}^{ij\tau s}$ is the FN of the geometrical stiffness matrix [57] arising from the nonlinear form of the strain-displacement geometrical relation, and the components of $\mathbf{K}_\sigma^{ij\tau s}$ are expressed in the following:

$$
\begin{aligned}
\mathbf{K}_\sigma^{ij\tau s}[1,1] &= <D_\sigma^{ij\tau s}+\tfrac{S_{\alpha\alpha}}{H_\alpha^2}\tfrac{F_\tau N_i F_s N_j}{R_\alpha^2}>, \quad \mathbf{K}_\sigma^{ij\tau s}[2,2] = <D_\sigma^{ij\tau s}+\tfrac{S_{\beta\beta}}{H_\beta^2}\tfrac{F_\tau N_i F_s N_j}{R_\beta^2}>,\\
\mathbf{K}_\sigma^{ij\tau s}[3,3] &= <D_\sigma^{ij\tau s}+\tfrac{S_{\alpha\alpha}}{H_\alpha^2}\tfrac{F_\tau N_i F_s N_j}{R_\alpha^2}+\tfrac{S_{\beta\beta}}{H_\beta^2}\tfrac{F_\tau N_i F_s N_j}{R_\beta^2}>,\\
\mathbf{K}_\sigma^{ij\tau s}[1,3] &= -\mathbf{K}_\sigma^{ij\tau s}[3,1] = <\tfrac{S_{\alpha\alpha}}{H_\alpha^2 R_\alpha}(F_\tau N_i F_s N_{j,\alpha}-F_\tau N_{i,\alpha}F_s N_j)\\
&+ \tfrac{S_{\alpha z}}{H_\alpha R_\alpha}(F_\tau N_i F_{s,z}N_j-F_{\tau,z}N_i F_s N_j)+\tfrac{S_{\alpha\beta}}{H_\alpha H_\beta R_\alpha}(F_\tau N_i F_s N_{j,\beta}-F_\tau N_{i,\beta}F_s N_j)>,\\
\mathbf{K}_\sigma^{ij\tau s}[2,3] &= -\mathbf{K}_\sigma^{ij\tau s}[3,2] = <\tfrac{S_{\beta\beta}}{H_\beta^2 R_\beta}(F_\tau N_i F_s N_{j,\beta}-F_\tau N_{i,\beta}F_s N_j)\\
&+ \tfrac{S_{\beta z}}{H_\beta R_\beta}(F_\tau N_i F_{s,z}N_j-F_{\tau,z}N_i F_s N_j)+\tfrac{S_{\alpha\beta}}{H_\alpha H_\beta R_\beta}(F_\tau N_i F_s N_{j,\alpha}-F_\tau N_{i,\alpha}F_s N_j)>,\\
\mathbf{K}_\sigma^{ij\tau s}[1,2] &= \mathbf{K}_\sigma^{ij\tau s}[2,1] = <\tfrac{S_{\alpha\beta}F_\tau N_i F_s N_j}{H_\alpha H_\beta R_\alpha R_\beta}>,
\end{aligned}
\tag{55}
$$

in which

$$
\begin{aligned}
D_{\sigma}^{ij\tau s} &= \frac{S_{\alpha\alpha}}{H_{\alpha}^{2}} F_{\tau} N_{i,\alpha} F_{s} N_{j,\alpha} + \frac{S_{\beta\beta}}{H_{\beta}^{2}} F_{\tau} N_{i,\beta} F_{s} N_{j,\beta} + S_{zz} F_{\tau,z} N_{i} F_{s,z} N_{j} \\
&+ \frac{S_{\alpha z}}{H_{\alpha}} \left(F_{\tau} N_{i,\alpha} F_{s,z} N_{j} + F_{\tau,z} N_{i} F_{s} N_{j,\alpha} \right) + \frac{S_{\beta z}}{H_{\beta}} \left(F_{\tau} N_{i,\beta} F_{s,z} N_{j} + F_{\tau,z} N_{i} F_{s} N_{j,\beta} \right) \\
&+ \frac{S_{\alpha\beta}}{H_{\alpha} H_{\beta}} \left(F_{\tau} N_{i,\alpha} F_{s} N_{j,\beta} + F_{\tau} N_{i,\beta} F_{s} N_{j,\alpha} \right) .
\end{aligned}
\tag{56}
$$

After $\mathbf{K}_{T_1}^{ij\tau s}$ and $\mathbf{K}_{\sigma}^{ij\tau s}$ are obtained, the FN of the tangent stiffness matrix $\mathbf{K}_{T}^{ij\tau s}$ is calculated straightforwardly from Eq. (49). Analogous to the secant stiffness matrix, the 3×3 FN can act as the basic building block to formulate the element and global tangent stiffness matrices for any higher-order and refined shell elements accounting for various kinematics and the full Green-Lagrange nonlinear strains.

5 Numerical examples and discussions

In this section, numerical calculations are carried out to demonstrate the capabilities of the developed full geometrically nonlinear CUF shell model to accurately predict the large-deflection, post-buckling and snapping equilibrium curves for some popular benchmark problems of nonlinear shell structures with different geometrical shapes, boundary and loading conditions as well as various sizes in a unified framework. The homogeneous isotropic metallic shell structures are taken into account as the first-step but effective verification of the CUF shell model by comparing our results with those provided in the literature. The total Lagrangian description along with the path-following Newton-Raphson method based on the arc-length constraint is utilized to compute all the numerical results. Note that depending on the actual number of iterations during the previous load step, the arc-length value can be automatically updated in each load step. The expansion functions along the thickness direction are based on the Lagrange polynomials, i.e., LE CUF shell models are used in this work. The acronym LDN representing the Lagrange expansion, Displacement-based theory with the order of expansion N will be employed to describe the refined CUF shell theories. In particular, the two-node linear (LD1), three-node quadratic (LD2), and four-node cubic (LD3) LE functions have been used in the following numerical investigations. If not otherwise stated, the FE analysis makes use of regular meshes of parabolic nine-node Lagrangian elements Q9 to approximate the displacement fields in the shell plane and all the numerical examples are based on the full Gauss integration scheme.

5.1 Post-buckling of a slender plate under compression

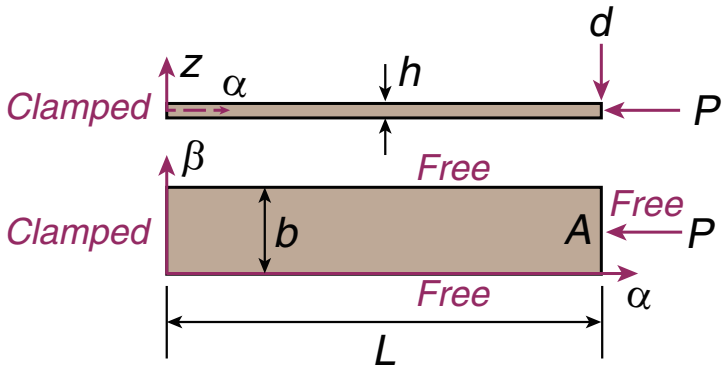

Figure 2: Schematic diagram of a clamped-free slender plate under the in-plane compressive point load P. Note that a small point load d is applied at the right free end to activate the post-buckling response.

The first numerical example is to show the enhanced abilities of the proposed full geometrically nonlinear unified shell model to provide an accurate prediction of the post-buckling equilibrium curves

for a slender plate subjected to the in-plane compression loading P, as shown in Fig. 2. This is a classical benchmark problem for the post-buckling analysis and has been considered by [24, 42]. For the purpose of illustration, the Young's modulus E_Y and Poisson's ratio ν of the slender plate adopted here are equal to $E_Y = 75$ GPa and $\nu = 0.316$. The length, width and thickness of the slender plate are assumed to be $L = 30$ cm, $b = 6$ cm and $h = 0.6$ cm, respectively. The clamped-free edge support conditions are applied to the slender plate. Specifically, the clamped edge condition satisfies $u_\alpha = u_\beta = u_z = 0$ at $\alpha = 0$, and the remaining edges are free of loadings. In addition, the point compression load P is applied at the point ($\alpha = L$, $\beta = b/2$, $z = 0$). In order to *activate* the stable branch along the post-buckling nonlinear path, a small disturbing point load d is applied at the free end ($\alpha = L$, $\beta = b/2$, $z = h/2$). The schematic diagram of the edge support conditions and loading states is displayed in Fig. 2.

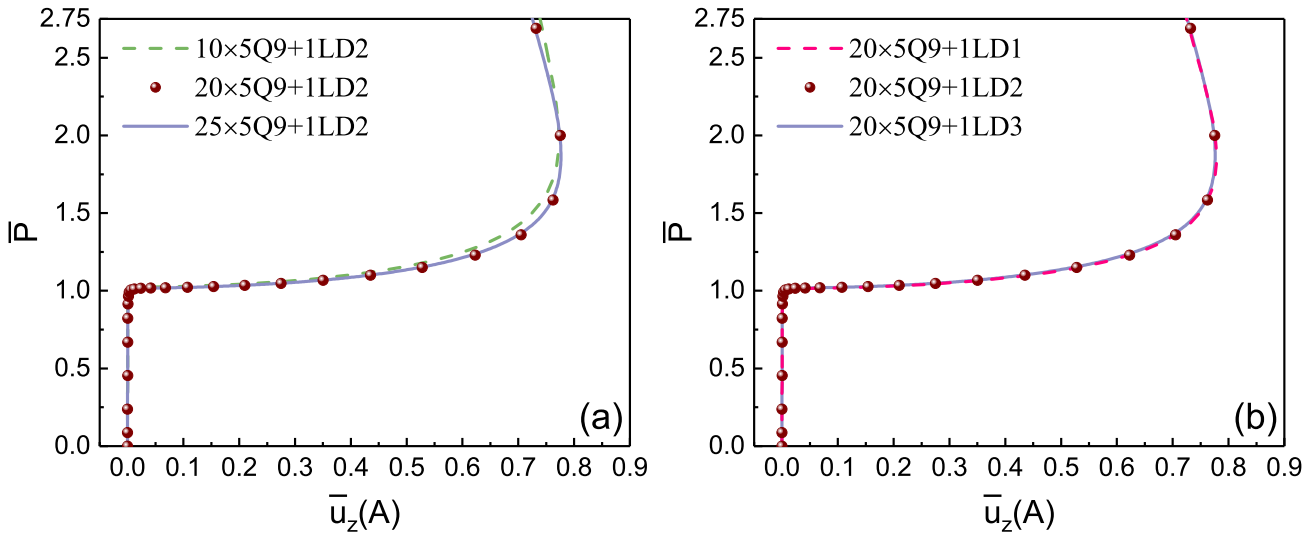

Figure 3: Convergence analysis of post-buckling equilibrium curves for the clamped-free isotropic slender plate under the in-plane compressive point load: (a) comparison of different in-plane mesh numbers; (b) comparison of various orders of Lagrange expansion functions in the thickness direction.

Now the convergence analysis of the present full geometrically nonlinear CUF shell model will be first conducted via a regular mesh for this example. Specifically, the post-buckling nonlinear response of the clamped-free slender plate to the applied compression loading P is shown in Fig. 3 for different in-plane mesh numbers (Fig. 3(a)) and various LE functions in the thickness direction (i.e., LD1, LD2 and LD3, as displayed in Fig. 3(b)), where the dimensionless maximum transverse deflection $\overline{u}_z(A) = u_z/L$, located at the plate center A, varies with the applied dimensionless in-plane compression load $\overline{P} = P(4L^2)/(\pi^2 EI_b)$, where $I_b = bh^3/12$. It can be seen from Fig. 3(a) that fairly fast convergence rate is obtained when increasing the number of the in-plane mesh. In addition, Fig. 3(b) demonstrates that all the lower and higher order CUF shell models can be employed to accurately predict the post-buckling equilibrium curves with the excellent convergence characteristic. Moreover, Fig. 3 illustrates that the critical buckling compression load P_{cr} of the slender plate is approximately equal to $\overline{P}_{cr} = P_{cr}(4L^2)/(\pi^2 EI_b) = 1.000$, where the classical Euler critical load for the cantilever beam subjected to compression has been used for normalization. Further, the present numerical results based on the CUF *shell* model also agree well with those using the full geometrically nonlinear CUF *plate* model in the work of Wu *et al.* [42].

In order to provide the convenient comparison with the reference solutions presented here, the equilibrium states of post-buckling response of the clamped-free slender plate under the in-plane compression based on different geometrically nonlinear CUF shell models are tabulated in Table 1 along with the total degrees of freedom (DOFs). Furthermore, based on the CUF kinematics $20 \times 5Q9 + 1LD2$, Fig. 4 depicts the kinematic evolution of the post-buckling pattern of the clamped-free slender plate under a series of different loadings, where the initial undeformed framework is also shown for the comparison purpose.

Table 1: Equilibrium points $(\overline{u}_z(A), \overline{P})$ of nonlinear response curves of the clamped-free slender plate under the in-plane compressive load based on different geometrically nonlinear CUF shell models.

Mesh number + Expansion order (DOFs)									
$10 \times 5Q9 + 1LD2$ (2079)		$20 \times 5Q9 + 1LD2$ (4059)		$25 \times 5Q9 + 1LD2$ (5049)		$20 \times 5Q9 + 1LD1$ (2706)		$20 \times 5Q9 + 1LD3$ (5412)	
$\overline{u}_z(A)$	$\overline{P}$	$\overline{u}_z(A)$	$\overline{P}$	$\overline{u}_z(A)$	$\overline{P}$	$\overline{u}_z(A)$	$\overline{P}$	$\overline{u}_z(A)$	$\overline{P}$
7.73E-6	0.08681	7.81E-6	0.08680	7.80E-6	0.08680	8.23E-6	0.08769	7.84E-6	0.08679
2.52E-5	0.23880	2.55E-5	0.23867	2.55E-5	0.23867	2.74E-5	0.24570	2.56E-5	0.23865
6.59E-5	0.45570	6.66E-5	0.45496	6.66E-5	0.45489	7.48E-5	0.47725	6.68E-5	0.45489
1.55E-4	0.67162	1.57E-4	0.66947	1.57E-4	0.66921	1.82E-4	0.69852	1.57E-4	0.66932
3.37E-4	0.82660	3.41E-4	0.82294	3.41E-4	0.82246	3.48E-4	0.82208	3.41E-4	0.82272
7.02E-4	0.91965	7.09E-4	0.91489	7.10E-4	0.91424	6.79E-4	0.90718	7.10E-4	0.91463
0.00143	0.97077	0.00145	0.96535	0.00145	0.96459	0.00134	0.95803	0.00145	0.96507
0.00289	0.99759	0.00292	0.99181	0.00293	0.99099	0.00267	0.98599	0.00292	0.99152
0.00582	1.01134	0.00587	1.00537	0.00589	1.00452	0.00532	1.00068	0.00588	1.00507
0.01166	1.01834	0.01178	1.01227	0.01180	1.01140	0.01061	1.00823	0.01178	1.01197
0.02335	1.02201	0.02358	1.01587	0.02362	1.01499	0.02121	1.01216	0.02358	1.01557
0.04086	1.02397	0.04126	1.01777	0.04133	1.01689	0.03708	1.01413	0.04127	1.01747
0.06707	1.02592	0.06773	1.01960	0.06785	1.01872	0.06086	1.01581	0.06774	1.01930
0.10621	1.02917	0.10724	1.02260	0.10744	1.02171	0.09638	1.01829	0.10726	1.02230
0.15277	1.03448	0.15425	1.02744	0.15452	1.02654	0.14922	1.02327	0.15427	1.02714
0.20784	1.04318	0.20982	1.03537	0.21019	1.03445	0.21162	1.03178	0.20986	1.03507
0.27239	1.05722	0.27492	1.04813	0.27540	1.04718	0.28449	1.04595	0.27497	1.04784
0.34701	1.07953	0.35012	1.06836	0.35071	1.06736	0.36813	1.06902	0.35018	1.06807
0.43142	1.11475	0.43507	1.10017	0.43577	1.09908	0.46154	1.10615	0.43514	1.09989
0.52359	1.17047	0.52768	1.15024	0.52846	1.14901	0.56125	1.16594	0.52776	1.14997
0.61842	1.25996	0.62274	1.23000	0.62357	1.22851	0.65957	1.26373	0.62284	1.22973
0.70564	1.40819	0.70500	1.36043	0.71080	1.35845	0.74225	1.4292	0.71012	1.36018
0.76738	1.66755	0.76204	1.58424	0.77266	1.58120	0.78646	1.72662	0.77210	1.58400
0.78008	2.06281	0.77518	1.99980	0.78359	1.99407	0.77169	2.19459	0.78320	1.99959
0.73448	2.84993	0.73171	2.68870	0.73206	2.67643	0.68874	3.16361	0.73167	2.68858

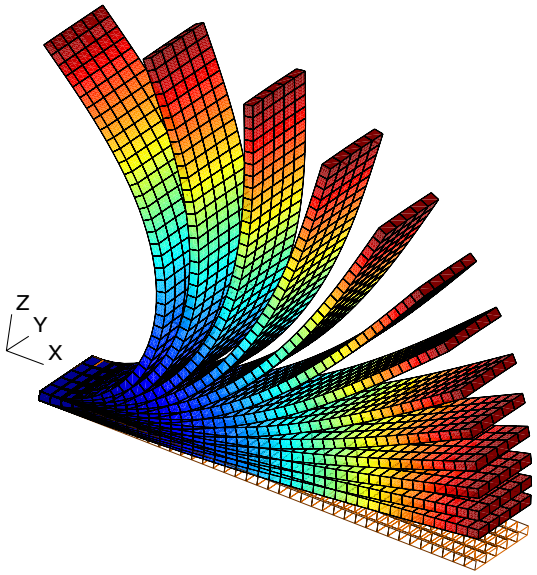

Figure 4: Some post-buckling configurations of the clamped-free slender plate under a series of in-plane compressive loads for various equilibrium states (the normalized loading forces $\overline{P} = 1.020, 1.023, 1.027, ..., 2.000, 2.689$). The initial undeformed framework of the slender plate is also shown.

5.2 Pinched semi-cylindrical shell

The second analysis deals with a clamped semi-cylindrical shell subjected to the point load P at the free end (see Fig. 5). This popular benchmark problem has been studied by [24, 59, 60, 61]. For representative purposes, the Young's modulus E_Y and the Poisson's ratio ν of the shell are set to be equal to $E_Y = 2.0685 \times 10^7$ and $\nu = 0.3$, respectively. The length, radius and thickness of the semi-cylindrical shell is $L = 3.048$, $R = 1.016$ and $h = 0.03$, respectively, corresponding to a thin shell. The clamped edge condition at $\beta = 0$ satisfies $u_\alpha = u_\beta = u_z = 0$ and along the longitudinal edges, all the circumferential deflections are constrained, i.e., $u_\alpha = 0$ at $\alpha = 0$ and $\alpha = \pi R$. The point load P is applied at the point A ($\alpha = \pi R/2$, $\beta = L$, $z = h/2$). The edge conditions are displayed in Fig. 5 along with the loading state. The symmetric condition enables to model half of the semi-cylindrical shell (see the shaded area in Fig. 5) to improve the computational efficiency, i.e., the symmetric boundary condition at $\alpha = \pi R/2$ fulfills $u_\alpha = 0$.

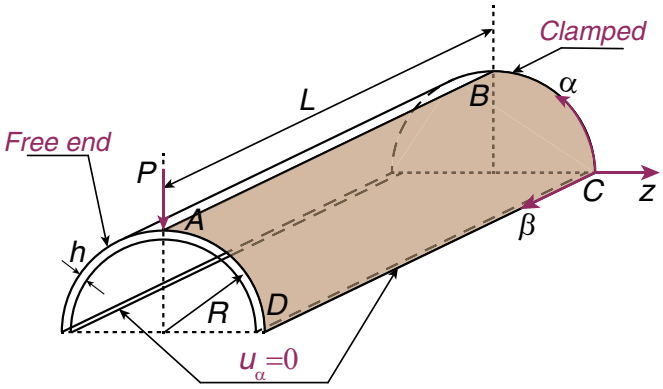

Figure 5: Schematic diagram of a clamped isotropic semi-cylindrical shell subjected to the point load at the free end (the boundary conditions along the longitudinal edges are also shown).

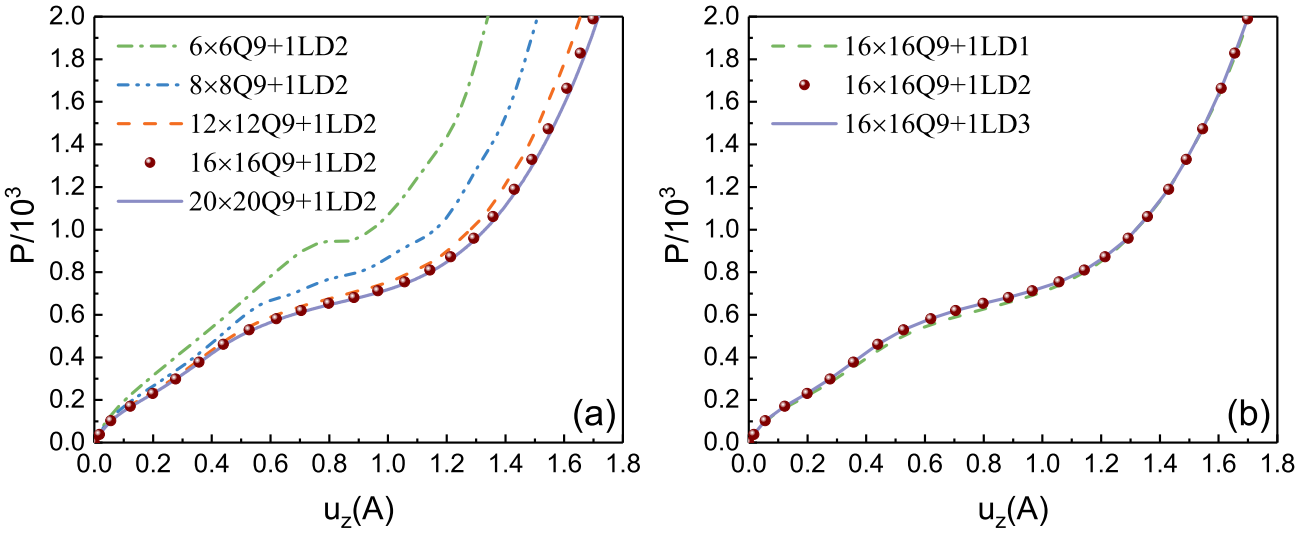

Figure 6: Convergence analysis of nonlinear response curves for the clamped isotropic semi-cylindrical shell under the point load: (a) comparison of different in-plane mesh numbers; (b) comparison of various orders of Lagrange expansion functions in the thickness direction.

First of all, the convergence analysis of the present CUF shell models is provided. To be specific, the large-deflection nonlinear curves for the clamped semi-cylindrical shell under the point load P is diplayed in Fig. 6 for comparison of different in-plane mesh numbers (Fig. 6(a)) and various LE functions in the thickness direction (i.e., LD1, LD2 and LD3, as shown in Fig. 6(b)). The equilibrium curves provide the downward deflections $u_z(A)$ at the point A as functions of the applied point force $P/10^3$. Obviously,

when increasing the in-plane mesh numbers to 16 × 16Q9, the results have an excellent convergence. Additionally, at least LD2 kinematics should be used to accurately predict the large-deflection equilibrium curves. Consequently, the kinematics 16 × 16Q9 + 1LD2 will be taken, for which the predicted large-deflection response to the point load can be assumed to have a high accuracy, as illustrated in Fig. 6. However, to provide the reference solutions of different in-plane meshes and expansion orders for future comparisons, the equilibrium points of large-deflection response of the clamped semi-cylindrical shell under the point force are tabulated in Tables 2 and 3 that also show the total DOFs.

Table 2: Equilibrium points $(u_z(A), P/10^3)$ of nonlinear response curves of the clamped isotropic semi-cylindrical shell under the point load based on geometrically nonlinear CUF shell models with *different in-plane mesh numbers*.

Mesh number + Expansion order (DOFs)												
12 × 12Q9 + 1LD2 (5625)				16 × 16Q9 + 1LD2 (9801)				20 × 20Q9 + 1LD2 (15129)			
$u_z(A)$	$P/10^3$	$u_z(A)$	$P/10^3$	$u_z(A)$	$P/10^3$	$u_z(A)$	$P/10^3$	$u_z(A)$	$P/10^3$	$u_z(A)$	$P/10^3$
0.01661	0.03836	1.13033	0.83312	0.01703	0.03837	1.05677	0.75441	0.01723	0.03837	1.07489	0.75483
0.07937	0.13465	1.17518	0.86918	0.05597	0.10341	1.14274	0.81010	0.08355	0.13391	1.13816	0.79545
0.17378	0.21708	1.21999	0.91978	0.12270	0.17061	1.21304	0.87272	0.18299	0.21573	1.19124	0.83812
0.28519	0.31479	1.27058	0.98675	0.19847	0.23067	1.29174	0.96022	0.29654	0.31553	1.25126	0.89705
0.40990	0.44405	1.31692	1.04637	0.27629	0.29922	1.35721	1.06181	0.40477	0.42338	1.30178	0.95837
0.53095	0.54976	1.36426	1.13242	0.35620	0.37836	1.42945	1.19003	0.52951	0.52555	1.35864	1.03929
0.67422	0.62589	1.41043	1.23601	0.43938	0.46141	1.48950	1.32976	0.66427	0.59618	1.40674	1.12266
0.74447	0.65723	1.45170	1.32381	0.52660	0.52987	1.54541	1.47355	0.72502	0.62080	1.46049	1.22720
0.82130	0.68183	1.48797	1.41756	0.61973	0.58193	1.60870	1.66354	0.78249	0.64133	1.50612	1.33323
0.89507	0.71181	1.52479	1.53552	0.70454	0.62029	1.65510	1.82883	0.84678	0.66207	1.58616	1.54758
0.96325	0.73470	1.56494	1.66733	0.79779	0.65377	1.69816	1.98973	0.90035	0.67987	1.65559	1.76792
1.02141	0.76256	1.59623	1.76147	0.88401	0.68178	1.74378	2.20869	0.96093	0.70140	1.69434	1.90422
1.07789	0.79972	1.63574	1.91704	0.96547	0.71299			1.01905	0.72616	1.72892	2.04882

Table 3: Equilibrium points $(u_z(A), P/10^3)$ of nonlinear response curves of the clamped isotropic semi-cylindrical shell under the point load based on geometrically nonlinear CUF shell models with *various expansion orders*.

Mesh number + Expansion order (DOFs)											
16 × 16Q9 + 1LD1 (6534)				16 × 16Q9 + 1LD2 (9801)				16 × 16Q9 + 1LD3 (13068)			
$u_z(A)$	$P/10^3$	$u_z(A)$	$P/10^3$	$u_z(A)$	$P/10^3$	$u_z(A)$	$P/10^3$	$u_z(A)$	$P/10^3$	$u_z(A)$	$P/10^3$
0.01841	0.03839	1.03686	0.72665	0.01703	0.03837	0.96547	0.71299	0.01706	0.03836	0.96581	0.71277
0.06052	0.10361	1.11920	0.78203	0.05597	0.10341	1.05677	0.75441	0.05612	0.10336	1.05712	0.75416
0.13269	0.17128	1.21137	0.86302	0.12270	0.17061	1.14274	0.81010	0.12295	0.17050	1.14308	0.80978
0.21441	0.23188	1.28605	0.95303	0.19847	0.23067	1.21304	0.87272	0.19874	0.23060	1.21341	0.87246
0.29796	0.30061	1.35670	1.05929	0.27629	0.29922	1.29174	0.96022	0.27654	0.29920	1.29210	0.95981
0.38350	0.37891	1.43577	1.20455	0.35620	0.37836	1.35721	1.06181	0.35645	0.37833	1.35759	1.06148
0.47250	0.45948	1.50073	1.35686	0.43938	0.46141	1.42945	1.19003	0.43964	0.46129	1.42984	1.18959
0.5660	0.52466	1.56114	1.51430	0.52660	0.52987	1.4895	1.32976	0.52688	0.52961	1.48988	1.32919
0.66585	0.57366	1.61842	1.68654	0.61973	0.58193	1.54541	1.47355	0.62002	0.58167	1.54582	1.47308
0.75674	0.61046	1.66615	1.85185	0.70454	0.62029	1.60870	1.66354	0.70485	0.62006	1.60910	1.66281
0.85706	0.64737	1.71162	2.02440	0.79779	0.65377	1.65510	1.82883	0.79811	0.65354	1.65553	1.82841
0.94990	0.68356	1.75840	2.24337	0.88401	0.68178	1.69816	1.98973	0.88434	0.68152	1.69857	1.98900

Furthermore, our numerical results predicted by the kinematics 16 × 16Q9 + 1LD2 are compared in Fig. 7 with the reference solution provided in Sze *et al.* [61], where the 40 × 40 S4R four-node shell elements in ABAQUS was used to calculate the large-deflection response for the same problem. It is noticed that the agreement of the present results with those of Sze *et al.* [61] is excellent. For the sake of completeness, some typical deformed configurations at three equilibrium states are illustrated in Fig. 8 for the clamped semi-cylindrical shell under the point load P. It must be underlined that the initial

undeformed framework of the semi-cylindrical shell is also illustrated in Fig. 8 for comparison purposes.

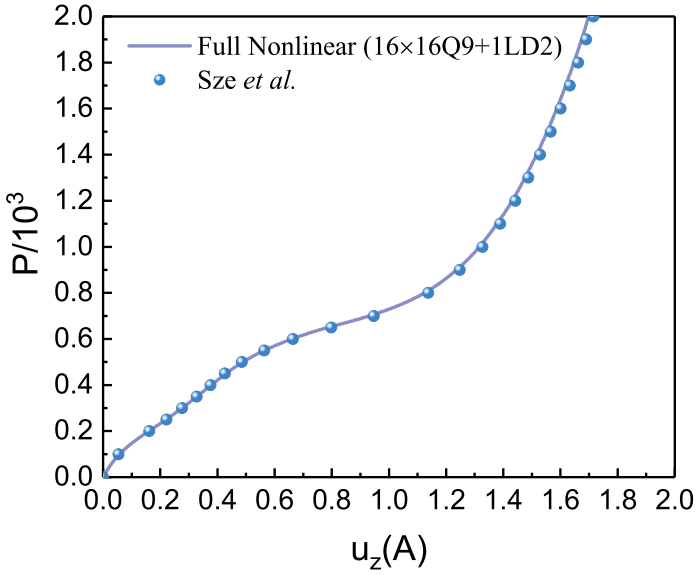

Figure 7: Nonlinear equilibrium curves of the clamped isotropic semi-cylindrical shell under the point load compared with the reference solution provided in Sze *et al.* [61].

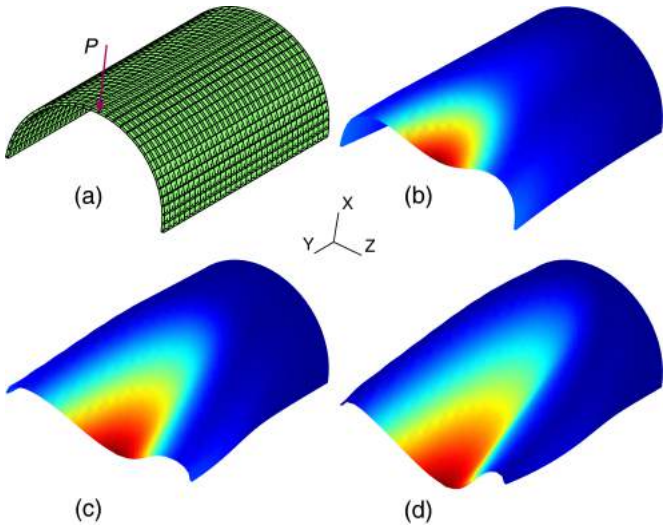

Figure 8: Some deformed configurations of the clamped semi-cylindrical shell under the point load P for three equilibrium states: (b) $u_z(A) = 0.7045, P/10^3 = 0.62$; (c) $u_z(A) = 1.4295, P/10^3 = 1.19$; (d) $u_z(A) = 1.7438, P/10^3 = 2.21$. The initial undeformed framework of the semi-cylindrical shell is also shown in Fig. 8(a).

5.3 Pull-out of an open-ended cylindrical shell

Next, an open-ended cylindrical shell subjected to a pair of radial pull-out point forces P (see Fig. 9) will be considered, which is a typical example to test the effectiveness of the FE formulations and has been investigated by [24, 59, 61, 62]. The material properties of the cylindrical shell used in this work are assumed to be $E_Y = 10.5 \times 10^6$ and $\nu = 0.3125$. Its length, radius and thickness are equal to $L = 10.35$, $R = 4.953$ and $h = 0.094$, respectively. The pull-out loads P are applied at points ($\alpha = 0$, $\beta = L/2$, $z = h/2$) and ($\alpha = \pi R$, $\beta = L/2$, $z = h/2$). The schematic diagram of boundary conditions and loading states is demonstrated in Fig. 9. Owing to the symmetry of the present problem, only an octant of the

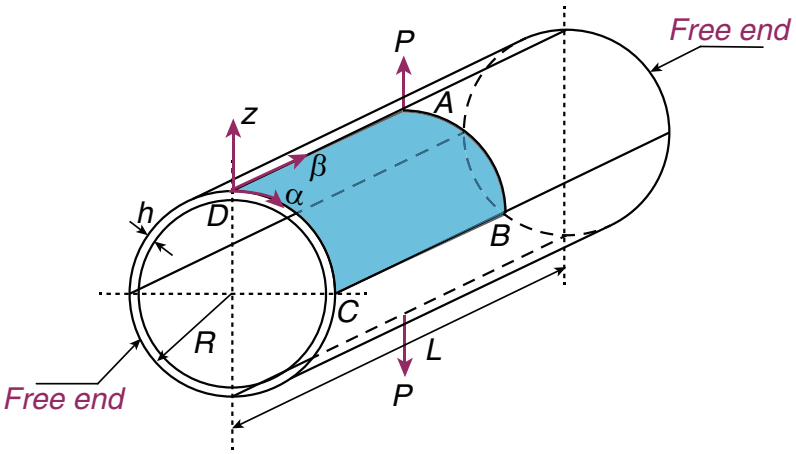

Figure 9: Schematic diagram of boundary conditions and loading states for an open-ended isotropic cylindrical shell subjected to pull-out point loads P.

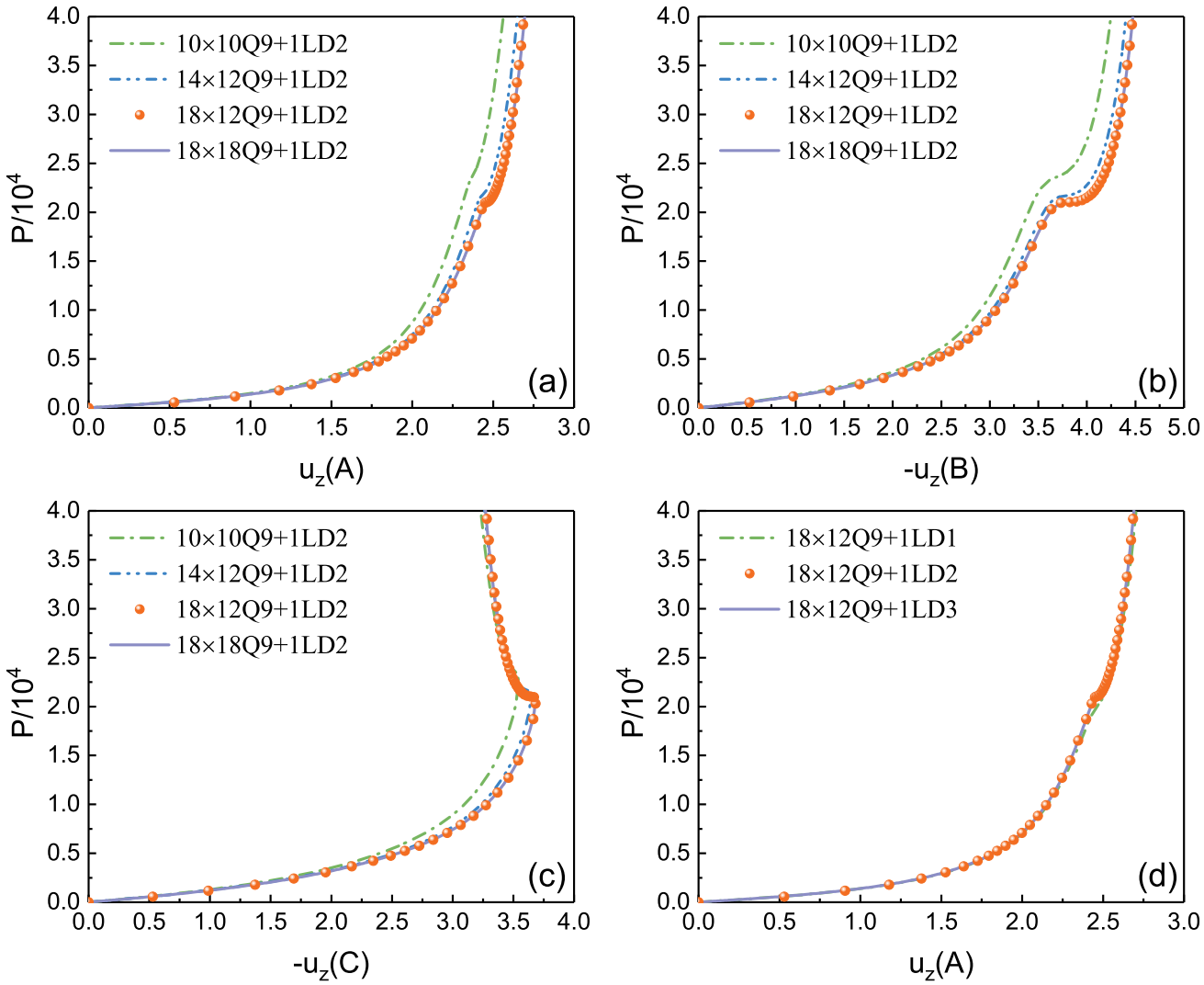

Figure 10: Convergence analysis of nonlinear response curves for the open-ended isotropic cylindrical shell subjected to pull-out point loads: (a-c) comparisons of different in-plane mesh numbers at points A, B and C depicted in Fig. 9; (b) comparison of various orders of Lagrange expansion functions in the thickness direction at point A.

cylindrical shell (see the shaded area in Fig. 9) is modeled to save the computing time, which makes the symmetric boundary conditions at $\alpha = 0$ and $\beta = L/2$ satisfy $u_\alpha = 0$ and $u_\beta = 0$, respectively.

Table 4: Equilibrium points $(u_z(A), P/10^4)$ of nonlinear response curves of the open-ended cylindrical shell subjected to pull-out point loads based on geometrically nonlinear CUF shell models with *different in-plane mesh numbers*.

Mesh number + Expansion order (DOFs)												
10×10Q9 + 1LD2 (3969)				14×12Q9 + 1LD2 (6525)				18×12Q9 + 1LD2 (8325)			
$u_z(A)$	$P/10^4$	$u_z(A)$	$P/10^4$	$u_z(A)$	$P/10^4$	$u_z(A)$	$P/10^4$	$u_z(A)$	$P/10^4$	$u_z(A)$	$P/10^4$
0.50151	0.05644	2.39316	2.43317	0.52305	0.05693	2.46311	2.23847	0.52898	0.05705	2.46996	2.10966
0.86219	0.11503	2.40106	2.46628	1.16593	0.17856	2.46868	2.25756	0.90557	0.11695	2.47985	2.12423
1.12421	0.17582	2.40970	2.50696	1.51173	0.30448	2.47455	2.27968	1.17753	0.17915	2.48915	2.14425
1.31702	0.23794	2.41904	2.55604	1.62356	0.36535	2.48072	2.30510	1.37717	0.24245	2.49748	2.16672
1.46091	0.30002	2.42908	2.61455	1.70933	0.42296	2.48719	2.33408	1.52613	0.30525	2.50472	2.18953
1.56979	0.36052	2.43979	2.68369	1.82795	0.52480	2.50098	2.40392	1.63897	0.36598	2.51241	2.21701
1.65321	0.41803	2.45115	2.76481	1.87889	0.57927	2.50829	2.44542	1.72558	0.42328	2.52053	2.24970
1.71781	0.47145	2.46317	2.85931	1.92890	0.64103	2.51585	2.49178	1.79283	0.47622	2.52908	2.28817
1.78027	0.53263	2.47581	2.96861	1.97822	0.71178	2.52367	2.54340	1.84557	0.52425	2.53804	2.33306
1.84085	0.60340	2.48907	3.09403	2.02712	0.79365	2.53174	2.60069	1.89720	0.57812	2.54739	2.38506
1.89989	0.68631	2.50289	3.23677	2.07583	0.88920	2.54005	2.66411	1.94797	0.63909	2.55712	2.44496
1.95784	0.78495	2.51726	3.39791	2.12454	1.00151	2.54859	2.73416	1.99813	0.70880	2.56722	2.51361
2.01521	0.90416	2.53212	3.57837	2.17338	1.13415	2.55735	2.81137	2.04792	0.78923	2.57767	2.59191
2.07253	1.05030	2.54740	3.77895	2.22247	1.29112	2.56633	2.89629	2.09754	0.88273	2.58846	2.68088
2.13024	1.23125	2.56306	4.00031	2.27181	1.47620	2.57553	2.98953	2.14715	0.99207	2.59958	2.78156
2.18865	1.45600	2.57903	4.24308	2.32111	1.69072	2.58494	3.09166	2.19687	1.12045	2.61101	2.89513
2.24768	1.73182	2.59525	4.50785	2.36002	1.87909	2.59456	3.20332	2.24675	1.27138	2.62274	3.02277
2.29479	1.98700			2.38926	2.02504	2.60437	3.32510	2.29678	1.44814	2.63476	3.16578
2.33010	2.19001			2.40902	2.11546	2.61438	3.45759	2.34669	1.65178	2.64707	3.32545
2.35279	2.30846			2.42066	2.15404	2.62457	3.60136	2.39529	1.87305	2.65965	3.50312
2.36547	2.35127			2.43920	2.17937	2.63495	3.75694	2.43010	2.03120	2.67250	3.70010
2.37513	2.37421			2.44405	2.18803	2.64549	3.92483	2.44967	2.09597	2.68559	3.91762
2.38441	2.40145			2.45293	2.20849	2.65619	4.10547	2.46017	2.10341	2.69893	4.15685

To clearly highlight the fairly fast and excellent convergence of the present full geometrically nonlinear CUF shell models, the large-deflection equilibrium curves for the open-ended cylindrical shell subjected to pull-out point loads P are shown in Fig. 10 for different in-plane mesh numbers (see Figs. 10(a)-(c)) and various LE functions (see Fig. 10(d)). In particular, the equilibrium curves give the radial displacements $u_z(A)$, $u_z(B)$ and $u_z(C)$ at points A, B and C in Fig. 9 as functions of the applied point load $P/10^4$. It can be found that the nonlinear response of the cylindrical shell is dominated by bending stiffness with large displacements before the point force of $P/10^4 = 2$, after which the large-deflection equilibrium curves are characterized by an extremely stiff response of the shell. In addition, it is obvious from Fig. 10 that the CUF shell model based on the kinematics 18×12Q9 + 1LD2 are able to predict the large-deflection nonlinear response to the pair of point loads with a high accuracy. Moreover, Tables 4 and 5 summarize the equilibrium points of the nonlinear response for different in-plane meshes and expansion orders, respectively, together with the total DOFs.

The converged solutions predicted by the 18×12Q9 + 1LD2 CUF shell model are compared in Fig. 11 with the results obtained by Sze *et al.* [61], who made use of the 24×36 S4R shell elements in the commercial code ABAQUS to calculate the large-deflection response for the same example. The CUF shell model results are in close agreement with those provided by Sze *et al.* [61] when $P/10^4 \lesssim 2$ but the present solutions provide *slightly stiffer* predictions for the three curves considered at points A, B and C in the highly nonlinear regime ($P/10^4 \gtrsim 2$). This is due to the fact that the S4R shell elements in ABAQUS are geometrically approximate based on an isoparametric approach by prescribing a unit normal at each node and also the von Kármán strain assumption is adopted. These approximations may fail to address the problems with large rotations and warping, which can be predicted by the present CUF shell model based on the exact geometrical nonlinear relations and pure displacement unknowns.

Table 5: Equilibrium points $(u_z(A), P/10^4)$ of nonlinear response curves of the open-ended cylindrical shell subjected to pull-out point loads based on geometrically nonlinear CUF shell models with *various expansion orders*.

Mesh number + Expansion order (DOFs)												
18×12Q9 + 1LD1 (5550)				18×12Q9 + 1LD2 (8325)				18×12Q9 + 1LD3 (11100)			
$u_z(A)$	$P/10^4$	$u_z(A)$	$P/10^4$	$u_z(A)$	$P/10^4$	$u_z(A)$	$P/10^4$	$u_z(A)$	$P/10^4$	$u_z(A)$	$P/10^4$
0.53142	0.05708	2.51557	2.14903	0.52898	0.05705	2.46996	2.10966	0.5292	0.05705	2.47076	2.10981
0.90954	0.11705	2.52596	2.19339	0.90557	0.11695	2.47985	2.12423	0.90593	0.11696	2.48067	2.12440
1.18258	0.17934	2.53696	2.24611	1.17753	0.17915	2.48915	2.14425	1.17800	0.17918	2.48998	2.14447
1.38305	0.24271	2.54853	2.30832	1.37717	0.24245	2.49748	2.16672	1.37770	0.24249	2.49833	2.16702
1.53272	0.30560	2.56066	2.38127	1.52613	0.30525	2.50472	2.18953	1.52671	0.30532	2.50558	2.18992
1.64618	0.36645	2.57334	2.46637	1.63897	0.36598	2.51241	2.21701	1.63959	0.36607	2.51329	2.21752
1.73338	0.42395	2.58654	2.56517	1.72558	0.42328	2.52053	2.24970	1.72624	0.42341	2.52143	2.25035
1.80120	0.47719	2.60026	2.67934	1.79283	0.47622	2.52908	2.28817	1.79351	0.47638	2.52999	2.28900
1.86714	0.53812	2.61446	2.81074	1.84557	0.52425	2.53804	2.33306	1.84626	0.52444	2.53897	2.33410
1.93159	0.60873	2.62914	2.96134	1.89720	0.57812	2.54739	2.38506	1.89791	0.57835	2.54834	2.38637
1.99500	0.69164	2.64428	3.13321	1.94797	0.63909	2.55712	2.44496	1.94870	0.63937	2.55809	2.44657
2.05777	0.79024	2.65988	3.32853	1.99813	0.70880	2.56722	2.51361	1.99888	0.70914	2.56820	2.51557
2.12027	0.90865	2.67591	3.54947	2.04792	0.78923	2.57767	2.59191	2.04870	0.78965	2.57867	2.59429
2.18275	1.05185	2.69236	3.79819	2.09754	0.88273	2.58846	2.68088	2.09835	0.88326	2.58948	2.68373
2.24535	1.22539	2.70921	4.07666	2.14715	0.99207	2.59958	2.78156	2.14798	0.99273	2.60061	2.78496
2.30797	1.43402	2.72643	4.38662	2.19687	1.12045	2.61101	2.89513	2.19772	1.12127	2.61207	2.89913
2.36964	1.67491	2.74400	4.72938	2.24675	1.27138	2.62274	3.02277	2.24764	1.27241	2.62382	3.02747
2.41545	1.86645			2.29678	1.44814	2.63476	3.16578	2.29770	1.44943	2.63587	3.17125
2.44356	1.96568			2.34669	1.65178	2.64707	3.32545	2.34764	1.65335	2.64820	3.33178
2.46019	1.99730			2.39529	1.87305	2.65965	3.50312	2.39625	1.87481	2.66080	3.51040
2.47527	2.02496			2.43010	2.03120	2.67250	3.70010	2.43103	2.03270	2.67367	3.70841
2.48996	2.06148			2.44967	2.09597	2.68559	3.91762	2.45050	2.09667	2.68679	3.92705
2.50353	2.10408			2.46017	2.10341	2.69893	4.15685	2.46096	2.10365	2.70015	4.16748

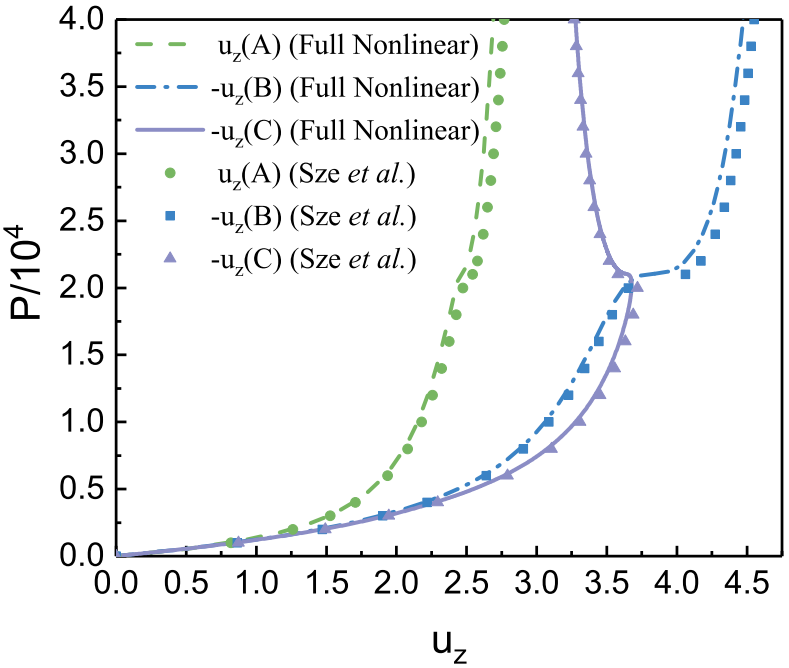

Figure 11: Nonlinear equilibrium curves (at points A, B and C depicted in Fig. 9) of the open-ended isotropic cylindrical shell subjected to pull-out point loads compared with the reference solution given in Sze *et al.* [61].

Furthermore, to better understand the kinematic evolution of the large-deflection response of the open-ended cylindrical shell subjected to pull-out point loads, six characteristic deformed configurations at equilibrium states are portrayed in Fig. 12. Note that only the semi-cylindrical shells are displayed and its initial undeformed frameworks are also illustrated simultaneously in Fig. 12.

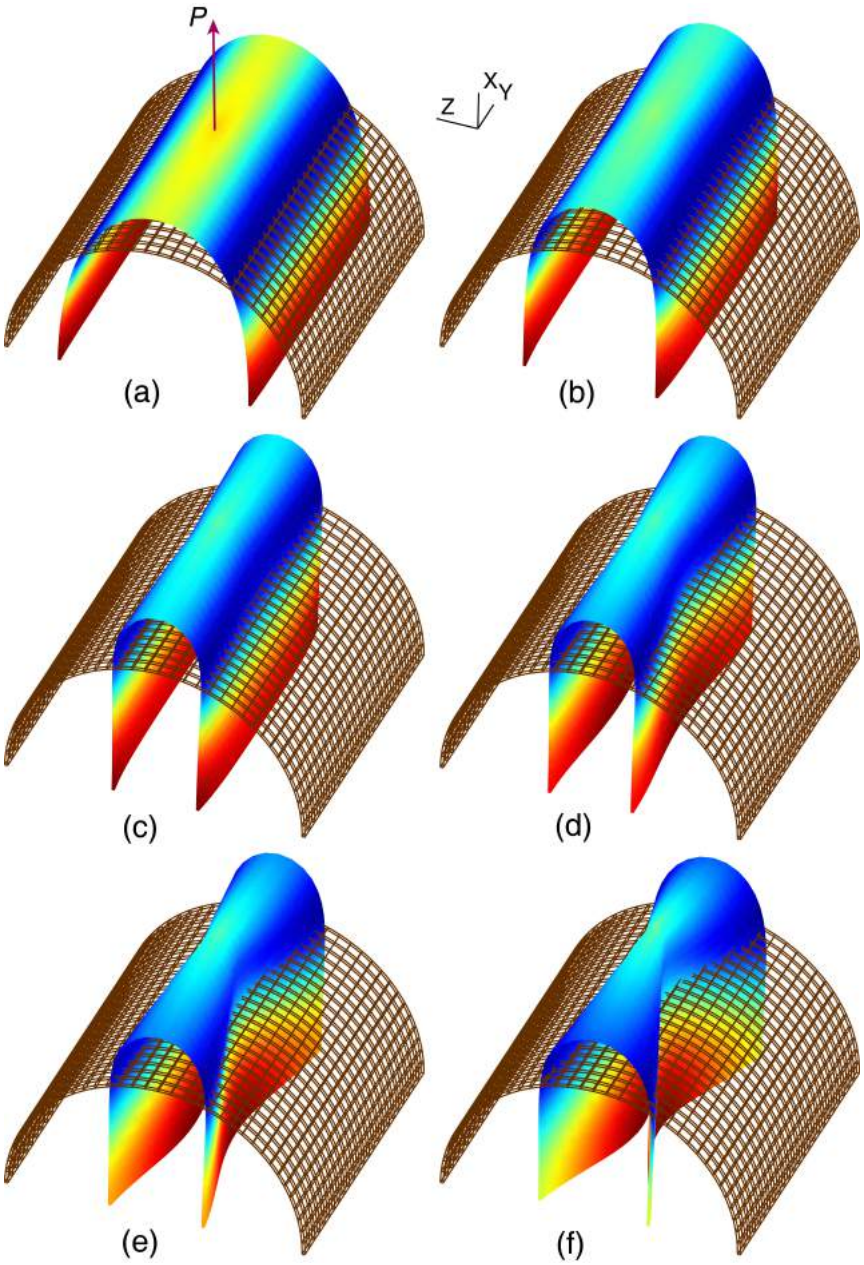

Figure 12: Some deformed configurations of the open-ended cylindrical shell subjected to pull-out point loads P for six equilibrium states: (a) $u_z(A) = 1.3772, P/10^4 = 0.24$; (b) $u_z(A) = 1.7256, P/10^4 = 0.42$; (c) $u_z(A) = 1.9480, P/10^4 = 0.64$; (d) $u_z(A) = 2.0975, P/10^4 = 0.88$; (e) $u_z(A) = 2.2968, P/10^4 = 1.45$; (f) $u_z(A) = 2.4700, P/10^4 = 2.11$. Note that only the semi-cylindrical shells are displayed and their initial undeformed frameworks are also shown.

5.4 Hinged cylindrical panel under point load

The next example considered here is a hinged elastic cylindrical shallow panel subjected to a central pinching force P, as shown in Fig. 13. This is a well-known benchmark problem and particularly popular due to the snapping behaviors, which means that the tangential global stiffness matrices become singular at some intermediate state. The problem has been computed by [24, 59, 61, 63, 64]. It should be

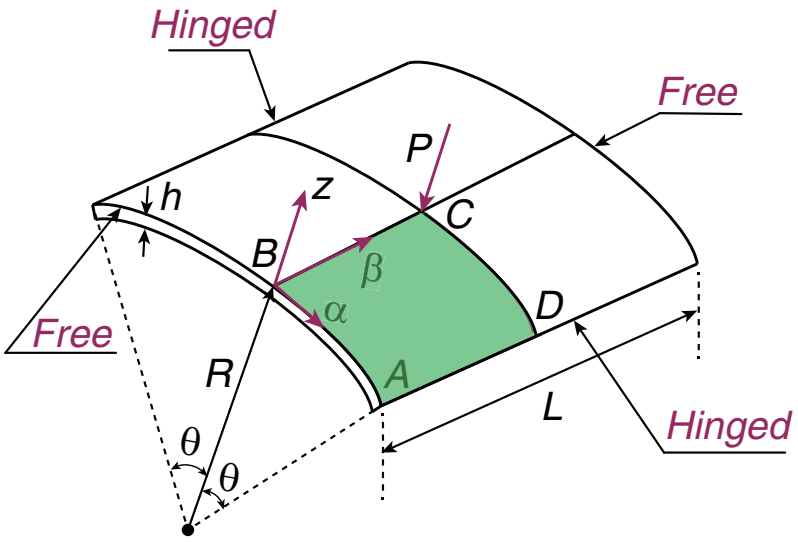

Figure 13: Schematic diagram of boundary conditions and loading states for a hinged isotropic cylindrical shallow panel under the point load P.

emphasized again that the path-following Newton-Raphson method based on the arc-length constraint is used to follow the nonlinear path and capture the limit points corresponding to the snap-through or snap-back phenomenon. The material properties of the isotropic cylindrical panel $E_Y = 3102.75$ N/mm^2 and $\nu = 0.3$ have been adopted with the geometrical data being $L = 508$ mm, $R = 2540$ mm, $\theta = 0.1$ rad and two different shell thicknesses $h = 12.7$ mm and $h = 6.35$ mm corresponding to moderately thick and thin shells. The panel is hinged at edges $\alpha = \pm R\theta$ satisfying $u_\alpha = u_\beta = u_z = 0$ at the mid-line $z = 0$ and free at edges $\beta = 0, L$. The point load P is applied at the point C ($\alpha = 0$, $\beta = L/2$, $z = h/2$). The edge conditions and loading state are shown in Fig. 13. The symmetric character enables to take a quarter of the cylindrical panel (see the shaded area in Fig. 13) as the computational domain. Thus, the symmetric boundary conditions at $\alpha = 0$ and $\beta = L/2$ fulfill $u_\alpha = 0$ and $u_\beta = 0$, respectively.

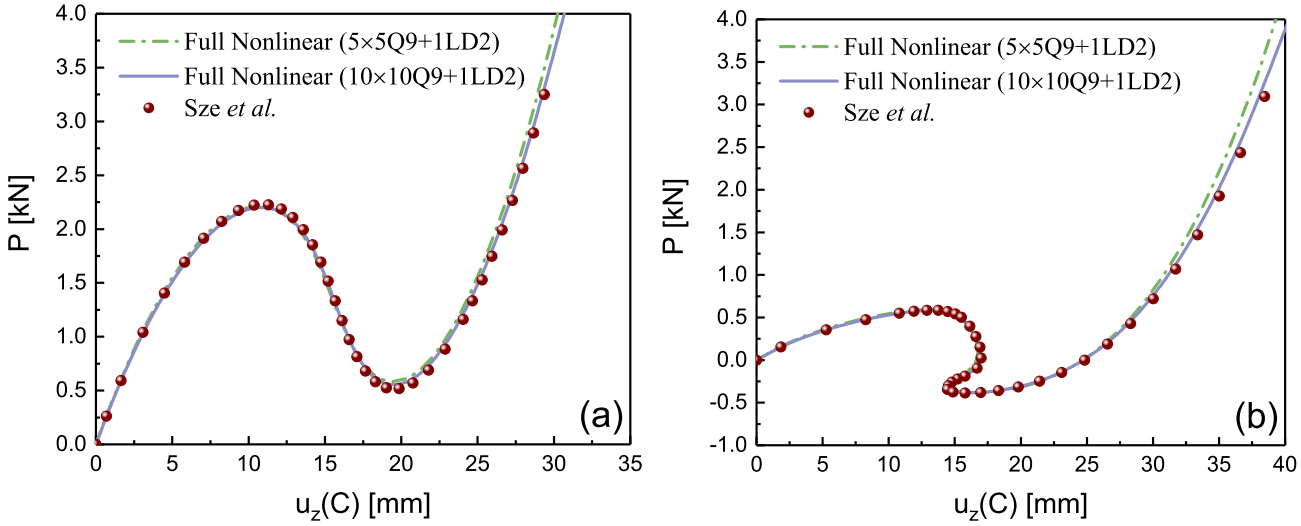

Figure 14: Convergence analysis of nonlinear equilibrium curves for the hinged isotropic cylindrical shallow panel under the point load compared with the reference solution provided in Sze *et al.* [61]: (a) 12.7 mm; (b) 6.35 mm.

Based on the present geometrically nonlinear CUF shell models (i.e., two in-plane mesh elements 5×5Q9 and 10×10Q9 as well as one quadratic (LD2) Lagrange polynomial are employed), the nonlinear equilibrium curves, providing the variations of the transverse deflection $u_z(C)$ at the central point with the central pinching force P, are illustrated in Figs. 14(a) and 14(b) for the hinged cylindrical panel

with thicknesses $h = 12.7$ mm and $h = 6.35$ mm, respectively. Adopting the 16×16 and 24×24 S4R shell elements as well as the Riks solution method in the commercial code ABAQUS, Sze *et al.* [61] also calculated the load-deflection curves of the cylindrical shallow panels with two thicknesses $h = 12.7$ mm and $h = 6.35$ mm, whose numerical results are exploited here in Fig. 14 for comparison purposes. It is rather clear that the present results shown in Fig. 14 obtained by the 10×10Q9 + 1LD2 CUF shell model are in complete agreement with those reported in Sze *et al.* [61] for the two shell thicknesses. Interestingly, the moderately thick cylindrical panel exhibits a limit point with the tangential matrix becoming singular (see Fig. 14(a)) and beyond the limit point, the nonlinear response of the panel will be unstable with a snap-through behavior, whereas the thinner panel displays a complex equilibrium path with not only horizontal but also vertical tangents with 0° and 90°, which correspond to the snap-through and snap-back phenomena, respectively. Similar to the previous examples, for the 5×5Q9 and 10×10Q9 + 1LD2 CUF shell models, Table 6 summarize the equilibrium points of the nonlinear response of the hinged cylindrical panel under point load with the moderately thick ($h = 12.7$ mm) and thin ($h = 6.35$ mm) thicknesses.

Table 6: Equilibrium points $(u_z(C), P)$ of nonlinear equilibrium curves of the hinged isotropic cylindrical shallow panel under point load based on geometrically nonlinear CUF shell models with *two different in-plane mesh numbers*. Note that the results are shown for both 12.7 mm and 6.35 mm thick cylindrical panels, and $u_z(C)$ and P are expressed in mm and kN.

Mesh number + Expansion order (DOFs)												
5×5Q9 + 1LD2 (1089)						10×10Q9 + 1LD2 (3969)					
$u_z(C)$	P	$u_z(C)$	P	$u_z(C)$	P	$u_z(C)$	P	$u_z(C)$	P	$u_z(C)$	P
(a) *12.7 mm moderately thick cylindrical panel*											
0.49422	0.19417	8.93350	2.14701	20.7310	0.58999	0.50964	0.19408	7.98502	2.02347	15.5031	1.38060
1.01929	0.39007	9.80375	2.20036	23.0090	0.94794	1.03809	0.38537	8.68809	2.09874	16.0075	1.17937
1.57634	0.58645	10.6752	2.21947	25.8366	1.77417	1.58540	0.57303	9.39238	2.15535	16.7547	0.91005
2.16634	0.78188	11.5364	2.19959	29.2210	3.29606	2.15150	0.75614	10.0937	2.19155	17.6665	0.68139
2.79007	0.97472	12.3746	2.13620	33.1598	5.83540	2.73615	0.93377	10.7872	2.20551	18.8512	0.54275
3.44800	1.16312	13.1769	2.02573			3.33897	1.10490	11.4677	2.19541	20.3947	0.55631
4.14019	1.34498	13.9337	1.86665			3.95939	1.26846	12.1294	2.15959	21.9415	0.73051
4.86623	1.51797	14.6441	1.66090			4.59658	1.42333	12.7666	2.09661	23.7841	1.10805
5.62504	1.67945	15.3244	1.41586			5.24947	1.56834	13.3744	2.00560	25.9316	1.75805
6.41474	1.82652	16.0184	1.14671			5.91669	1.70223	13.9493	1.88649	28.3883	2.76964
7.23242	1.95594	17.1093	0.79560			6.59650	1.82367	14.4912	1.74041	31.1565	4.25732
8.07390	2.06409	18.6028	0.56003			7.28681	1.93125	15.0051	1.57015		
(b) *6.35 mm thin cylindrical panel*											
1.53098	0.14062	16.6499	0.21722	17.5801	-0.37722	1.61952	0.13978	16.8069	0.18385	17.4074	-0.37414
3.21266	0.26088	16.8009	0.07590	18.3942	-0.36376	3.37952	0.25796	16.8038	-0.06282	18.1195	-0.36211
5.02749	0.36168	16.6132	-0.03845	19.3716	-0.33917	5.25390	0.35638	16.2702	-0.14414	18.9720	-0.34204
6.94749	0.44629	16.0812	-0.12070	20.5368	-0.29734	7.20918	0.43898	15.5468	-0.19652	19.9894	-0.30974
8.93548	0.51703	15.3709	-0.17254	21.9141	-0.22828	8.72831	0.49289	14.9532	-0.23533	21.1975	-0.25843
10.4636	0.56036	14.7941	-0.21085	23.5251	-0.11608	10.2941	0.53941	14.6401	-0.27287	22.6214	-0.17729
12.0087	0.59077	14.5318	-0.24939	25.3872	0.06337	11.8672	0.57361	14.5040	-0.30799	24.2823	-0.04979
13.1509	0.59902	14.4938	-0.28668	27.5144	0.34495	13.0249	0.58533	14.4895	-0.33728	26.1963	0.14815
13.9812	0.59157	14.5707	-0.31867	29.9225	0.77773	14.1136	0.57633	14.7440	-0.36437	28.3767	0.45027
14.7490	0.56595	14.8348	-0.35064	32.6338	1.43074	15.0372	0.53591	15.2349	-0.37829	30.8396	0.90332
15.3986	0.51634	15.4478	-0.37488	35.6811	2.40183	15.5942	0.48014	15.7870	-0.38351	33.6089	1.57267
15.9137	0.44041	16.1807	-0.38375	39.1086	3.83050	16.0600	0.40163	16.3221	-0.38364	36.7188	2.55064
16.3258	0.33978	16.9068	-0.38329	42.9723	5.91606	16.4659	0.30227	16.8143	-0.38076	40.2150	3.96824

Moreover, to clearly demonstrate the kinematic evolution of the nonlinear response of the cylindrical shallow panel subjected to the point load, some characteristic deformed configurations at three notable equilibrium states for the thickness $h = 12.7$ mm are depicted in Fig. 15, where the initial undeformed framework is separately illustrated in Fig. 15(a) for comparison. As we can see, despite the high nonlinearity for this problem, the maximum deflection is much smaller than the overall dimensions of the panel, i.e., no large displacements and rotations occur during the nonlinear response. Therefore, the

S4R shell elements in ABAQUS based on the FSDT and the von Kármán assumption can provide good approximations for this example with moderate rotations. Note that this classical problem is merely used for the first-step effective verification of the proposed CUF shell model and it cannot immediately reflect the superior advantages of the full geometrically nonlinear unified shell model that will be discussed in Sec. 6.

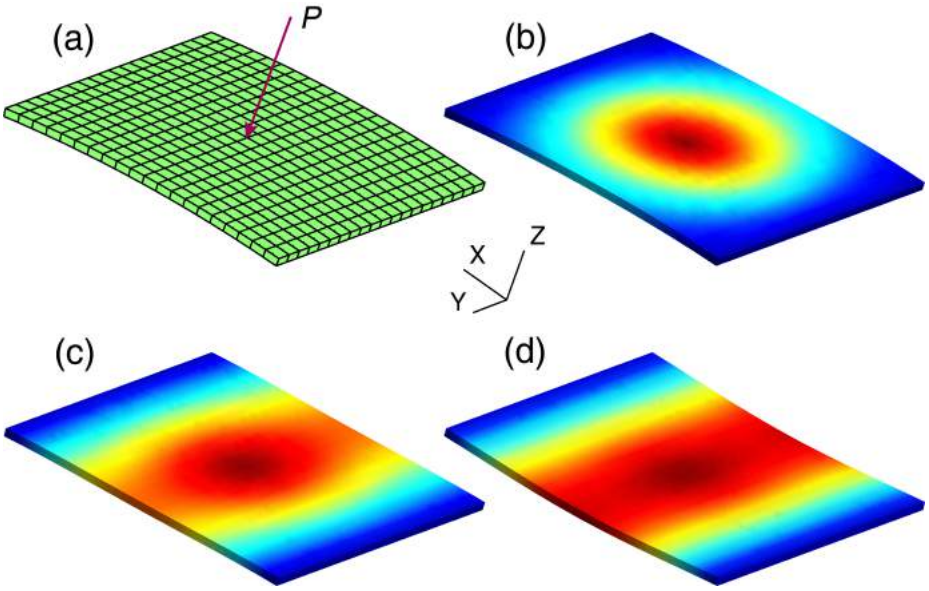

Figure 15: Some deformed configurations of the hinged cylindrical shallow panel under the point load P for three equilibrium states: (b) $u_z(C) = 7.2868$ mm, $P = 1.93$ kN; (c) $u_z(C) = 13.3744$ mm, $P = 2.01$ kN; (d) $u_z(C) = 18.8512$ mm, $P = 0.54$ kN. The initial undeformed framework of the panel is also shown in Fig. 15(a).

5.5 Beam-like cylindrical arch

As a finial example, an elastic beam-like cylindrical shallow arch subjected to a point load P at the mid-span (see Fig. 16) is studied. The adopted material properties of the isotropic cylindrical arch are the same as those in Subsec. 5.4. The geometrical sizes are equal to $R = 2540$ mm, $\theta = 0.1$ rad, $h = 12.7$ mm and $b = 10.16$ mm, where b is the width of the beam-like cylindrical arch. Two kinds of surpport conditions at edges $\alpha = 0$ and $2R\theta$ will be considered: (1) the *hinged* boundary conditions satisfying $u_\alpha = u_\beta = u_z = 0$ at the mid-line $z = 0$ and (2) the *fixed* boundary conditions fulfilling $u_\alpha = u_\beta = u_z = 0$ at the whole cross section. The point load P is applied at the point C ($\alpha = R\theta$, $\beta = b/2$, $z = h/2$). The boundary conditions and loading state are depicted in Fig. 16.

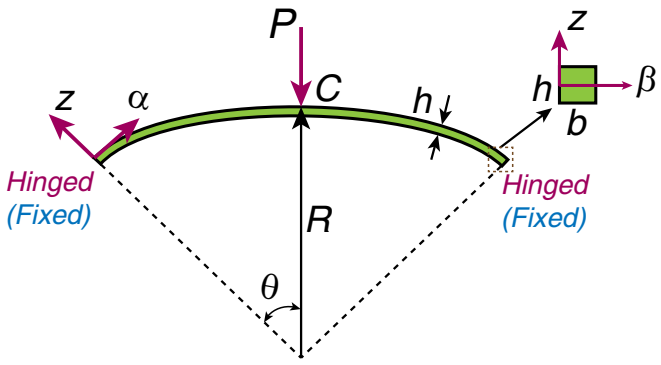

Figure 16: Schematic diagram of boundary conditions and loading states for a beam-like isotropic cylindrical arch under the point load P.

After the convergence analysis, the 20 × 1Q9 +1LD2 CUF shell model is employed to compute the nonlinear equilibrium curves for the hinged and fixed beam-like cylindrical arches under the point load, as shown in Fig. 17 that illustrates the transverse deflection $u_z(C)$ at the central point as functions of the central point force P. As we can see, the nonlinear response of the hinged beam-like arch exhibits a snap-through behavior at some intermediate state, similar to the previous results in Subsec. 5.4, whereas that of the fixed beam-like arch demonstrates a monotonically increasing variation without the snap-through phenomenon. This difference is believed to be due to the fact that, compared with the hinged arch, the fixed one cannot withstand the rotations at both ends, which is also clearly shown in Fig. 18.

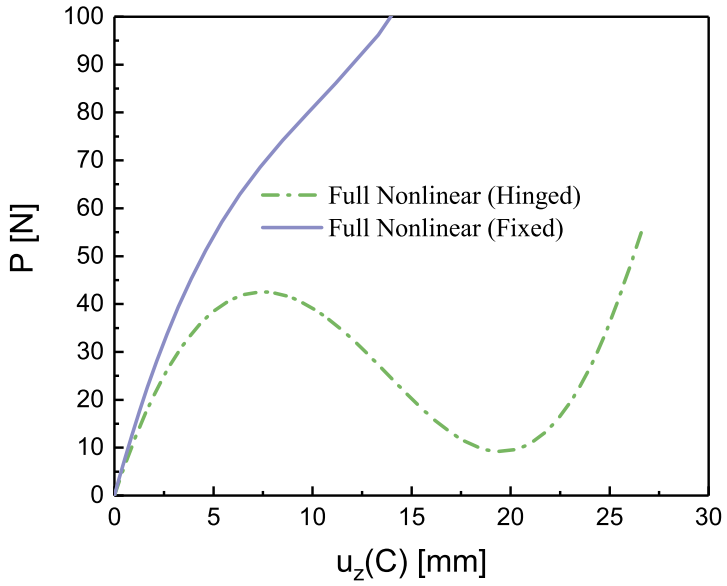

Figure 17: Nonlinear equilibrium curves for the beam-like isotropic cylindrical arch under point load with the hinged and fixed boundary conditions.

For the hinged and fixed beam-like cylindrical arches under a central point load, Table 7 tabulates the equilibrium points of their nonlinear responses based on the 20 × 1Q9 + 1LD2 CUF shell model for the future reference. Further, the kinematic evolution of some notable deformed configurations at equilibrium states are depicted in Fig. 18 for both the hinged and fixed beam-like cylindrical arches subjected to the central point load, where the initial undeformed frameworkes are also illustrated in Fig. 18 for comparison purposes.

Table 7: Equilibrium points $(u_z(C), P)$ of nonlinear equilibrium curves of the beam-like isotropic cylindrical arch under point load with the *hinged and fixed* boundary conditions based on the geometrically nonlinear CUF shell model. Note that $u_z(C)$ and P are expressed in mm and N.

Mesh number + Expansion order (DOFs) = 20 × 1Q9 + 1LD2 (1107)											
Hinged								*Fixed*			
$u_z(C)$	P	$u_z(C)$	P	$u_z(C)$	P	$u_z(C)$	P	$u_z(C)$	P	$u_z(C)$	P
0.31761	3.88570	4.14844	35.0658	9.38396	40.5780	17.2315	12.2876	0.26143	3.92604	5.42311	57.1081
0.64616	7.67893	4.60393	37.0457	9.99592	39.1866	18.3772	9.78003	0.55464	8.16041	6.33452	62.9068
0.98599	11.3651	5.07381	38.7482	10.6253	37.4343	19.5787	8.83521	0.88343	12.7027	7.35311	68.5950
1.33740	14.9292	5.55836	40.1562	11.2727	35.3365	20.8432	10.1150	1.25207	17.5452	8.49082	74.2171
1.70072	18.3551	6.05786	41.2533	11.9388	32.9179	22.1774	14.4078	1.66532	22.6714	9.76084	79.9365
2.07626	21.6267	6.57257	42.0244	12.6245	30.2149	23.5872	22.6475	2.12846	28.0547	11.1779	86.1090
2.46435	24.7271	7.10277	42.4553	13.3309	27.2778	25.0773	35.9368	2.64740	33.6567	13.3174	96.2282
2.86530	27.6389	7.64872	42.5342	14.0594	24.1745	26.6517	55.5769	3.22867	39.4273	15.6986	
3.27942	30.3445	8.21071	42.2514	15.0790	19.8910			3.87954	45.3053	18.3517	
3.70703	32.8261	8.78901	41.6002	16.1344	15.8080			4.60806	51.2220	21.3137	

6 Conclusions

In this work a unified formulation of full geometrically nonlinear refined shell theory is developed based on the Carrera Unified Formulation (CUF) and the total Lagrangian approach. In particular, the linear and nonlinear differential operator matrices in the geometrical relation is obtained explicitly in the orthogonal parallel curvilinear coordinate system via the tensor calculus. The fundamental nuclei (FNs) of the secant and tangent stiffness matrices of the shell element with geometrical nonlinearities are derived in a unified way owing to the scalable characteristics of CUF. Some benchmark numerical assessments are conducted by utilizing the path-following Newton-Raphson linearization scheme along with the arc-length constraint, which is especially suitable for the nonlinear analysis of post-buckling and snapping phenomena. The convergence analyses of these popular benchmark problems are executed for different in-plane mesh numbers and various expansion orders of Lagrange functions in the thickness direction. Sufficient data points for different kinematic assumptions are tabulated in numerical format to accurately reconstruct the relevant load-deflection curves and to provide the reference solutions for future comparisons of the new finite element models. The excellent agreement with the numerical solutions from the literatures manifests the validation and the enhanced accuracy of the proposed CUF shell model to predict the large-deflection, post-buckling, snap-through and snap-back nonlinear responses of flexible shell structures.

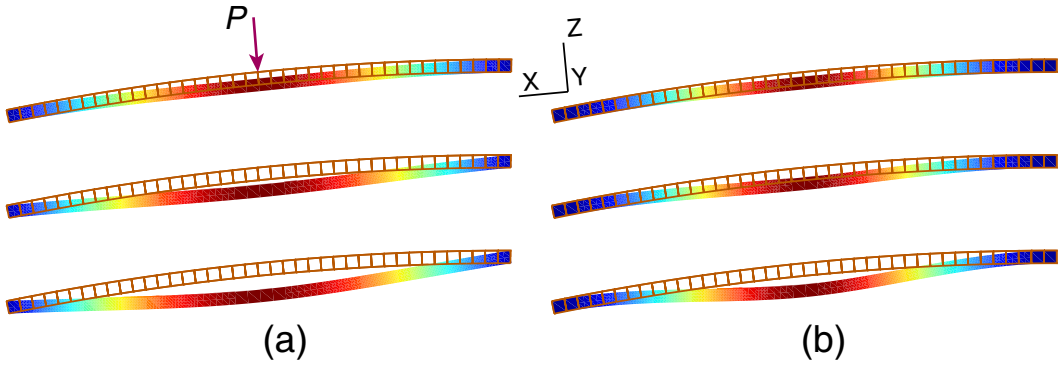

Figure 18: Some deformed configurations of the beam-like cylindrical arch under the point load P with different boundary conditions: (a) hinged (loading forces $P = 42.02, 12.29$ and 55.58 N); (b) fixed (loading forces $P = 51.22, 79.94$ and 172.00 N). The initial undeformed frameworks are also depicted in Figs. 18(a) and 18(b).

In addition to the accurate predictions of the nonlinear responses of flexible structures, the present full geometrically nonlinear refined shell model possesses some other advantages: (i) The nonlinear governing equations of the CUF shell models are expressed by the fundamental nuclei and can be obtained in a unified and general manner, which enables to automatically adjust the model efficiency/efficacy depending on the complexity of the problem under consideration; (ii) In principle, the nonlinear higer-order CUF model can accurately predict the nonlinear internal stress states of composite structures [47]; (iii) Owing to the scalable behaviors, the full geometrically nonlinear CUF model can be conveniently harnessed to assess the effectiveness of different geometrically nonlinear strain approximations [47]. These aspects are not available for other analytical and numerical methods in the literature. The analyses of points (ii) and (iii) for anisotropic composite shell structrues are now under way.

Acknowledgements

This work was supported by the awarding of Research Fellow at Politecnico di Torino, the Government of Ireland Postdoctoral Fellowship from the Irish Research Council (No. GOIPD/2019/65), the Russian Science Foundation (No. 18-19-00092), and the National Natural Science Foundation of China (Nos. 11872329 and 11621062). Partial supports from the Fundamental Research Funds for the Central Universities, PR China (No. 2016XZZX001-05) and the Shenzhen Scientific and Technological Fund for

R&D, PR China (No. JCYJ20170816172316775) are also acknowledged.

References

[1] W. T. Koiter. On foundations of linear theory of thin elastic shells. *Proceedings of the Koninklijke Nederlandse Akademie van Wetenschappen Series B-Physical Sciences*, 73(3):169–195, 1970.

[2] P. M. Naghdi. *Theory of shells and plates.* in: S. Flügge, C. Truesdell (Eds.), Handbuch der Physik, Vol. VIa/2, Springer-Verlag, Berlin, 1972.

[3] A. N. Palazotto. *Nonlinear analysis of shell structures.* AIAA Education Series, 1992.

[4] J. N. Reddy. *Mechanics of Laminated Composite Plates and Shells: Theory and Analysis.* CRC Press, 2003.

[5] E. Carrera, M. Cinefra, M. Petrolo, and E. Zappino. *Finite Element Analysis of Structures through Unified Formulation.* John Wiley & Sons, Chichester, West Sussex, UK, 2014.

[6] R. K. Kapania and S. Raciti. Recent advances in analysis of laminated beams and plates. Part I: Shear effects and buckling. *AIAA Journal*, 27(7):923–935, 1989.

[7] E. Carrera. Historical review of zig-zag theories for multilayered plates and shells. *Applied Mechanics Reviews*, 56(3):287–308, 2003.

[8] W. M. Sokolowski and S. C. Tan. Advanced self-deployable structures for space applications. *Journal of Spacecraft and Rockets*, 44(4):750–754, 2007.

[9] M. Amabili. *Nonlinear Mechanics of Shells and Plates in Composite, Soft and Biological Materials.* Cambridge University Press, New York, USA, 2018.

[10] K. Bertoldi, V. Vitelli, J. Christensen, and M. van Hecke. Flexible mechanical metamaterials. *Nature Reviews Materials*, 2(11):17066, 2017.

[11] B. Wu, W. J. Zhou, R. H. Bao, and W. Q. Chen. Tuning elastic waves in soft phononic crystal cylinders via large deformation and electromechanical coupling. *Journal of Applied Mechanics*, 85(3):031004, 2018.

[12] Y. J. Chen, B. Wu, Y. P. Su, and W. Q. Chen. Tunable two-way unidirectional acoustic diodes: Design and simulation. *Journal of Applied Mechanics*, 86(3):031010, 2019.

[13] E. Carrera and B. Kröplin. Zigzag and interlaminar equilibria effects in large-deflection and post-buckling analysis of multilayered plates. *Mechanics of Composite Materials and Structures*, 4(1):69–94, 1997.

[14] C. Y. Chia. *Nonlinear Analysis of Plates.* McGraw-Hill, New York, 1980.

[15] A. W. Leissa. Buckling of laminated composite plates and shell panels. *Flight Dynamics Laboratory Report*, AFWAL-TR-85-3069, 1985.

[16] B. Budiansky. Notes on nonlinear shell theory. *Journal of Applied Mechanics*, 35:393–401, 1968.

[17] R. Schmidt. A current trend in shell theory: Constrained geometrically nonlinear Kirchhoff–Love type theories based on polar decomposition of strains and rotations. *Computers & Structures*, 20:265–275, 1985.

[18] C. Y. Chia. Geometrically nonlinear behavior of composite plates: A review. *Applied Mechanics Reviews*, 41(12):439–451, 1988.

[19] L. Librescu and M. Stein. Postbuckling of shear deformable composite flat panels taking into account geometrical imperfections. *AIAA Journal*, 30(5):1352–1360, 1992.

[20] E. Carrera and M. Villani. Large deflections and stability FEM analysis of shear deformable compressed anisotropic flat panels. *Composite Structures*, 29(4):433–444, 1994.

[21] E. Carrera and M. Villani. Effects of boundary conditions on postbuckling of compressed, symmetrically laminated thick plates. *AIAA Journal*, 33(8):1543–1546, 1995.

[22] C. Sansour. A theory and finite element formulation of shells at finite deformations involving thickness change: Circumventing the use of a rotation tensor. *Archive of Applied Mechanics*, 65(3):194–216, 1995.

[23] M. Bischoff and E. Ramm. Shear deformable shell elements for large strains and rotations. *International Journal for Numerical Methods in Engineering*, 40(23):4427–4449, 1997.

[24] R. A. Arciniega and J. N. Reddy. Tensor-based finite element formulation for geometrically nonlinear analysis of shell structures. *Computer Methods in Applied Mechanics and Engineering*, 196(4-6):1048–1073, 2007.

[25] G. S. Payette and J. N. Reddy. A seven-parameter spectral/hp finite element formulation for isotropic, laminated composite and functionally graded shell structures. *Computer methods in applied mechanics and engineering*, 278:664–704, 2014.

[26] M. G. Rivera, J. N. Reddy, and M. Amabili. A new twelve-parameter spectral/hp shell finite element for large deformation analysis of composite shells. *Composite Structures*, 151:183–196, 2016.

[27] J. N. Reddy. A refined nonlinear theory of plates with transverse shear deformation. *International Journal of Solids and Structures*, 20(9-10):881–896, 1984.

[28] N. S. Putcha and J. N. Reddy. A refined mixed shear flexible finite element for the nonlinear analysis of laminated plates. *Composite Structures*, 20(4):273–282, 1986.

[29] C. T. Tsai and A. N. Palazotto. A modified riks approach to composite shell snapping using a high-order shear deformation theory. *Computers & Structures*, 35(3):221–226, 1990.

[30] L. Librescu and M. Y. Chang. Imperfection sensitivity and postbuckling behavior of shear-deformable composite doubly-curved shallow panels. *International Journal of Solids and Structures*, 29(9):1065–1083, 1992.

[31] M. Amabili and J. N. Reddy. A new non-linear higher-order shear deformation theory for large-amplitude vibrations of laminated doubly curved shells. *International Journal of Non-Linear Mechanics*, 45(4):409–418, 2010.

[32] M. Amabili. Non-linearities in rotation and thickness deformation in a new third-order thickness deformation theory for static and dynamic analysis of isotropic and laminated doubly curved shells. *International Journal of Non-Linear Mechanics*, 69:109–128, 2015.

[33] S. Ahmad, B. M. Irons, and O. C. Zienkiewicz. Analysis of thick and thin shell structures by curved finite elements. *International Journal for Numerical Methods in Engineering*, 2(3):419–451, 1970.

[34] N. Buechter and E. Ramm. Shell theory versus degeneration - A comparison in large rotation finite element analysis. *International Journal for Numerical Methods in Engineering*, 34(1):39–59, 1992.

[35] E. Carrera and S. Brischetto. Analysis of thickness locking in classical, refined and mixed theories for layered shells. *Composite Structures*, 85(1):83–90, 2008.

[36] H. Parisch. A continuum-based shell theory for non-linear applications. *International Journal for Numerical Methods in Engineering*, 38(11):1855–1883, 1995.

[37] J. N. Reddy and J. Kim. A nonlinear modified couple stress-based third-order theory of functionally graded plates. *Composite Structures*, 94(3):1128–1143, 2012.

[38] M. Amabili. A non-linear higher-order thickness stretching and shear deformation theory for large-amplitude vibrations of laminated doubly curved shells. *International Journal of Non-Linear Mechanics*, 58:57–75, 2014.

[39] R. Schmidt and J. N. Reddy. A refined small strain and moderate rotation theory of elastic anisotropic shells. *Journal of Applied Mechanics*, 55:611–617, 1988.

[40] D. Kim and R. A. Chaudhuri. Full and von Kármán geometrically nonlinear analyses of laminated cylindrical panels. *AIAA Journal*, 33(11):2173–2181, 1995.

[41] E. Carrera and H. Parisch. An evaluation of geometrical nonlinear effects of thin and moderately thick multilayered composite shells. *Composite Structures*, 40(1):11–24, 1997.

[42] B. Wu, A. Pagani, M. Filippi, W. Q. Chen, and E. Carrera. Large-deflection and post-buckling analyses of isotropic rectangular plates by carrera unified formulation. *International Journal of Non-Linear Mechanics*, 116:18–31, 2019.

[43] H. B. Coda. Continuous inter-laminar stresses for regular and inverse geometrically nonlinear dynamic and static analyses of laminated plates and shells. *Composite Structures*, 132:406–422, 2015.

[44] F. Alijani and M. Amabili. Non-linear static bending and forced vibrations of rectangular plates retaining non-linearities in rotations and thickness deformation. *International Journal of Non-Linear Mechanics*, 67:394–404, 2014.

[45] A. Pagani and E. Carrera. Unified formulation of geometrically nonlinear refined beam theories. *Mechanics of Advanced Materials and Structures*, 25(1):15–31, 2018.

[46] A. Pagani and E. Carrera. Large-deflection and post-buckling analyses of laminated composite beams by Carrera Unified Formulation. *Composite Structures*, 170:40–52, 2017.

[47] B. Wu, A. Pagani, M. Filippi, W. Q. Chen, and E. Carrera. Accurate stress fields of post-buckled laminated composite beams accounting for various kinematics. *International Journal of Non-Linear Mechanics*, 111:60–71, 2019.

[48] P. F. Pai. *Highly Flexible Structures: Modeling, Computation, and Experimentation.* AIAA Education Series, Reston, VA, 2007.

[49] A. H. Nayfeh and P. F. Pai. *Linear and Nonlinear Structural Mechanics.* John Wiley & Sons, 2008.

[50] E. Carrera, G. Giunta, and M. Petrolo. *Beam Structures: Classical and Advanced Theories.* John Wiley & Sons, 2011.

[51] A. E. Green and W. Zerna. *Theoretical Elasticity, Second Edition.* Clarendon Press, Oxford, 1968.

[52] K. J. Bathe. *Finite Element Procedure.* Prentice Hall, Upper Saddle River, New Jersey, USA, 1996.

[53] J. N. Reddy. *An Introduction to Nonlinear Finite Element Analysis: With Applications to Heat Transfer, Fluid Mechanics, and Solid Mechanics.* Oxford University Press, Oxford, 2014.

[54] M. A. Crisfield. A fast incremental/iterative solution procedure that handles "snap-through". *Computers & Structures*, 13(1):55–62, 1981.

[55] M. A. Crisfield. An arc-length method including line searches and accelerations. *International Journal for Numerical Methods in Engineering*, 19(9):1269–1289, 1983.

[56] E. Carrera. A study on arc-length-type methods and their operation failures illustrated by a simple model. *Computers & Structures*, 50(2):217–229, 1994.

[57] O. C. Zienkiewicz and R. L. Taylor. *The Finite Element Method for Solid and Structural Mechanics*. Butterworth-Heinemann, Washington, 6th edition, 2005.

[58] M. A. Crisfield. *Non-Linear Finite Element Analysis of Solid and Structures*. John Wiley & Sons, Chichester, England, 1991.

[59] B. Brank, F. B. Damjanić, and D. Perić. On implementation of a nonlinear four node shell finite element for thin multilayered elastic shells. *Computational Mechanics*, 16(5):341–359, 1995.

[60] M. Balah and H. N. Al-Ghamedy. Finite element formulation of a third order laminated finite rotation shell element. *Computers & Structures*, 80(26):1975–1990, 2002.

[61] K. Y. Sze, X. H. Liu, and S. H. Lo. Popular benchmark problems for geometric nonlinear analysis of shells. *Finite Elements in Analysis and Design*, 40(11):1551–1569, 2004.

[62] C. Sansour and F. G. Kollmann. Families of 4-node and 9-node finite elements for a finite deformation shell theory. an assesment of hybrid stress, hybrid strain and enhanced strain elements. *Computational Mechanics*, 24(6):435–447, 2000.

[63] A. Barut, E. Madenci, and A. Tessler. Nonlinear analysis of laminates through a mindlin-type shear deformable shallow shell element. *Computer Methods in Applied Mechanics and Engineering*, 143(1-2):155–173, 1997.

[64] S. J. Lee and W. Kanok-Nukulchai. A nine-node assumed strain finite element for large-deformation analysis of laminated shells. *International Journal for Numerical Methods in Engineering*, 42(5):777–798, 1998.